Available online at www.sciencedirect.com
ScienceDirect
Comput. Methods Appl. Mech. Engrg. 197 (2008) 2789–2803
Computer methods in applied mechanics and engineering
www.elsevier.com/locate/cma

Assumed enhanced strain and the extended finite element methods: A unification of concepts

Ronaldo I. Borja

Department of Civil and Environmental Engineering, Stanford University, Stanford, CA 94305, USA

Received 25 September 2007; received in revised form 24 December 2007; accepted 14 January 2008
Available online 9 February 2008

Abstract

We present strong and weak forms of boundary-value problems for a solid with a cohesive–frictional crack. Two commonly used techniques for enhancing the finite element (FE) interpolation are considered: the assumed enhanced strain (AES) and the extended FE methods. We compare and contrast the FE approximations involved in these techniques. The AES method employs a piecewise constant interpolation of slip that is discontinuous across element boundaries. In contrast, the extended FE method interpolates slip continuously across element boundaries. Through numerical examples, we discuss the implications of these approximations to the calculated overall deformation field in the regime of infinitesimal deformation. With only a Heaviside enrichment, we find the AES method to predict larger slip (i.e., softer response) compared to the extended FE solution. We ascribe the discrepancy to the lack of higher-order crack tip enhancement in the extended FE solution. Finally, we compare the slip predicted by the above FE enhancement techniques to that calculated by classical nonlinear contact mechanics algorithm for the case where the crack traverses the element sides.

Keywords: Assumed enhanced strain; Embedded strong discontinuity; Extended finite element method; Frictional crack

1. Introduction

Over the past two decades there has been a steady stream of publications in the computational mechanics literature dealing with the topics of material failure and damage. A class of problems that has attracted enormous attention involves large deformation occurring over a very narrow zone, see e.g., [1–35]. Deformation bands are narrow zones of intense shear, compaction, and/or dilation [36–47]. On a macroscopic scale the displacement field is continuous but the strain field inside the band is intense. Faults are highly damaged gouge zones where granulized particles roll and slide past each other even as the material outside this zone remains relatively undamaged. The effective friction coefficient along a fault depends on lithology, presence of fluids, temperature, and the evolving thickness of the gouge produced by continued slip and wear along contact surfaces [36,48–50,52–54]. Fractures or cracks are much narrower zones of intense deformation, approaching a discontinuous displacement field where two surfaces either separate or slide past each other [44,48,51,55,56]. The coefficient of friction in frictional fractures or cracks have been observed from laboratory experiments to vary with slip speed and maturity of contact [57–60].

Because of nearly overlapping definitions, qualitative descriptions of failure modes are quite artificial, and actual mechanism of deformation could involve combinations of several far more complex processes. However, in this paper we distinguish between two mechanisms of deformation: a continuum strain localization mode in which the two sides of damage zone are in direct physical contact; and a separation mode characterized by a pair of traction-free surfaces. Deformation bands, faults, and frictional cracks are examples of a continuum strain localization mode; opening mode fractures, sometimes simply called cracks, are examples of a separation mode. The distinction is made since two very prominent finite element (FE) enhancement

E-mail address: borja@stanford.edu

0045-7825/$ - see front matter © 2008 Elsevier B.V. All rights reserved.
doi:10.1016/j.cma.2008.01.019

techniques, the assumed enhanced strain (AES) and the extended FE methods, have emerged at their inception to capture these two respective mechanisms of deformation.

A mathematical foundation of the AES method may be traced to Simo and Rifai [28], who used a three-field Hu–Washizu variational formulation for strain enhancements to improve the performance of lower-order "locking" elements, i.e., elements which exhibit stiff responses owing to their inability to capture some kinematical features of deformation such as bulk incompressibility and bending. Conforming finite elements have difficulty capturing localized deformation, so the AES method also has been tailored to improve element performance for such application. It must be noted that the AES method was developed primarily for continuum strain localization problems, and not for opening mode fractures. In the former application the gradient of slip on the band in the direction of the axis of the band is relatively small and hence is ignored in the AES formulation. Furthermore, the tip of the band is usually a fracture process zone where localized deformation is smeared throughout the element volume. An appealing feature of the AES formulation is that no additional global degrees of freedom are required since the element enhancement is purely local. Static condensation is a procedure typically used to eliminate the element enhancement prior to global assembly. Furthermore, for constant strain triangular elements, static condensation may be done just as effectively at the Gauss point level, leading to a so-called Galerkin embedded strong discontinuity algorithm [3]. The latter method mimics the classical smeared crack approaches [61–64] and can be implemented using the platform for standard continuum plasticity requiring no modification to the element subroutine, i.e., changes reflecting the post-localization responses are restricted to the material subroutine only.

The past decade has seen the emergence of an enhancement technique called the extended FE method for crack propagation simulation. In principle, the technique introduces the enhancement to allow a conforming finite element to separate into two parts. The method is based on partition of unity [65,66] and permits a continuous interpolation of discontinuity across element boundaries. Early applications of the extended FE formulations have focused on opening mode fractures where the tractions on the free surfaces are zero. Because of the assumption of free tractions, the formulation naturally leads to a kinematical problem under compression when contact condition could not be enforced without causing the free surfaces to overlap.

Very limited work has been done to address contact condition and cohesive–frictional crack propagation in the context of the extended FE method. Dolbow et al. [8] imposed the contact constraint for frictional crack propagation through a variational formulation expressed in terms of the total displacements of the discontinuity surfaces. Their formulation requires that the two surfaces be iteratively "closed" to enforce contact condition using an iterative algorithm called LATIN [67]. Unfortunately, this iterative algorithm converges very slowly and does not permit machine precision accuracy. Kim et al. [17] proposed an improved version utilizing Newton's method along with so-called 'mortared elements' as a regularization scheme. Liu and Borja [20] reformulated the frictional crack propagation problem in terms of relative displacement of the sliding surfaces using a penalty algorithm borrowed from nonlinear contact mechanics [68–70], along with Newton iteration. The rapid convergence rate of Newton iteration allows machine precision accuracy in the global nonlinear equation solve, while the penalty formulation for contact condition allows tracking of the path-dependent incremental solution.

In this paper, we elucidate the concepts underlying the AES and the extended FE methods with reference to frictional crack propagation simulation. To limit the scope of the paper, opening mode fracture is not covered in this work. We emphasize that the aim of this paper is to unify the underlying concepts and not to give a historical perspective of the aforementioned methods. To make the exposition complete, we have implemented the above methods in a common FE platform, along with classical contact mechanics algorithm [68–70], so that we may compare quantitatively the solutions provided by each of these methods. Theoretical formulations are first presented, including the strong and weak forms of the boundary value problem. We next differentiate between the Petrov–Galerkin and Bubnov–Galerkin FE formulations employed in the AES and extended FE methods, respectively. Focusing on slip patterns, we show that the asymptotic FE solutions produced by the AES and extended FE methods differ substantially particularly near the crack tip. We attribute the discrepancy to the lack of a special crack tip enhancement needed by the extended FE solutions to fully capture the strain singularity at the crack tip.

2. Variational formulation

We consider a body Ω with a surface of discontinuity $\mathscr{S}$ shown in Fig. 1. In order for the comparison of the methods to be more transparent, we shall express all relevant variables in rate form. The velocity field $\boldsymbol{v}(\boldsymbol{x})$ is discontinuous on $\mathscr{S}$ according to the equation

$$\boldsymbol{v}(\boldsymbol{x}) = \bar{\boldsymbol{v}}(\boldsymbol{x}) + M_{\mathscr{S}}(\boldsymbol{x})\tilde{\boldsymbol{v}}(\boldsymbol{x}), \tag{1}$$

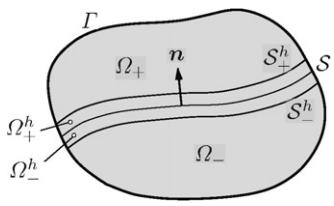

Fig. 1. Definition of problem domain and boundaries. Domain Ω is cut by a surface of discontinuity $\mathscr{S}$ into Ω_- and Ω_+. Compact support of $M_{\mathscr{S}}(\boldsymbol{x})$ is $\Omega^h = \Omega_-^h \cup \Omega_+^h$, and bounded by surfaces $\mathscr{S}_\pm^h$. Unit normal vector to $\mathscr{S}$ is $\boldsymbol{n}$, pointing in the direction of Ω_+.

where $\bar{\boldsymbol{v}}(\boldsymbol{x})$ and $M_{\mathscr{S}}(\boldsymbol{x})\tilde{\boldsymbol{v}}(\boldsymbol{x})$ are the continuous and discontinuous parts of $\boldsymbol{v}(\boldsymbol{x})$, respectively. The scalar function $M_{\mathscr{S}}(\boldsymbol{x})$ generates the discontinuity on the surface $\mathscr{S}$, and is given by the equation

$$M_{\mathscr{S}}(\boldsymbol{x}) = H_{\mathscr{S}}(\boldsymbol{x}) - f^h(\boldsymbol{x}), \tag{2}$$

where $H_{\mathscr{S}}(\boldsymbol{x})$ is the Heaviside function defined by

$$H_{\mathscr{S}}(\boldsymbol{x}) = \begin{cases} 1, & \boldsymbol{x} \in \Omega_+ \\ 0, & \boldsymbol{x} \in \Omega_- \end{cases} \tag{3}$$

and $f^h(\boldsymbol{x})$ is any arbitrary smooth 'blending' function that satisfies the following requirements

$$f^h(\boldsymbol{x})\tilde{\boldsymbol{v}}(\boldsymbol{x}) = \begin{cases} \boldsymbol{0} & \text{on } \mathscr{S}^h_- \cup (\Omega_- \setminus \Omega^h_-), \\ \tilde{\boldsymbol{v}}(\boldsymbol{x}) & \text{on } \mathscr{S}^h_+ \cup (\Omega_+ \setminus \Omega^h_+). \end{cases} \tag{4}$$

The discontinuous part of velocity satisfies the properties

$$\operatorname{supp}[M_{\mathscr{S}}(\boldsymbol{x})\tilde{\boldsymbol{v}}(\boldsymbol{x})] = \Omega^h_- \cup \Omega^h_+, \quad [\![M_{\mathscr{S}}(\boldsymbol{x})\tilde{\boldsymbol{v}}(\boldsymbol{x})]\!] = \tilde{\boldsymbol{v}}(\boldsymbol{x})|_{\mathscr{S}}, \tag{5}$$

where "supp" stands for support of a function, and $[\![\cdot]\!]$ denotes a jump. The blending function $f^h(\boldsymbol{x})$ adds elegance to the formulation since it allows the nodal displacements calculated at the global level to be accepted as the final displacements. The function $f^h(\boldsymbol{x})$ also plays a key role in the definition of the equivalent weighting function for use with the AES method.

Restricting the discussion to infinitesimal deformation, we write the strain rate tensor as

$$\dot{\boldsymbol{\epsilon}} = \boldsymbol{\nabla}^{\mathrm{s}}\boldsymbol{v} = \boldsymbol{\nabla}^{\mathrm{s}}\bar{\boldsymbol{v}} + H_{\mathscr{S}}(\boldsymbol{x})\boldsymbol{\nabla}^{\mathrm{s}}\tilde{\boldsymbol{v}} - \boldsymbol{\nabla}^{\mathrm{s}}(f^h(\boldsymbol{x})\tilde{\boldsymbol{v}}) + \delta_{\mathscr{S}}(\tilde{\boldsymbol{v}} \otimes \boldsymbol{n})^{\mathrm{s}}, \tag{6}$$

where $\boldsymbol{\nabla}^{\mathrm{s}}$ is the symmetric spatial gradient operator, $(\cdot)^{\mathrm{s}}$ denotes the symmetric part of the tensor, and $\delta_{\mathscr{S}}$ is the Dirac delta distribution function.

Without loss of generality we assume quasi-static loading and write the governing equations in rate form as follows:

$$\operatorname{div}(\dot{\boldsymbol{\sigma}}) + \dot{\boldsymbol{f}} = \boldsymbol{0} \quad \text{in } \Omega \setminus \mathscr{S}, \tag{7}$$

$$\boldsymbol{v} \cdot \dot{\boldsymbol{\sigma}} = \dot{\boldsymbol{t}} \quad \text{on } \Gamma_{\boldsymbol{t}}, \tag{8}$$

where $\dot{\boldsymbol{\sigma}}$ is the Cauchy stress rate tensor, $\dot{\boldsymbol{f}}$ is the body force rate vector, $\dot{\boldsymbol{t}}$ is the traction rate vector acting on external surface boundary $\Gamma_{\boldsymbol{t}}$, and $\boldsymbol{v}$ is the unit normal vector to $\Gamma_{\boldsymbol{t}}$. For dead loading $\dot{\boldsymbol{f}} = \dot{\boldsymbol{t}} = \boldsymbol{0}$. We augment the above equations with the following conditions on the surface of discontinuity

$$\boldsymbol{n} \cdot \dot{\boldsymbol{\sigma}} = \dot{\boldsymbol{t}}_{\mathscr{S}_-} \quad \text{on } \mathscr{S}_-, \tag{9}$$

$$-\boldsymbol{n} \cdot \dot{\boldsymbol{\sigma}} = \dot{\boldsymbol{t}}_{\mathscr{S}_+} \quad \text{on } \mathscr{S}_+ \tag{10}$$

in which $\boldsymbol{n}$ is the unit normal vector to $\mathscr{S}$ and pointing toward Ω_+, see Fig. 1.

Consistent with the velocity field (1), we assume a family of weighting functions of the form:

$$\boldsymbol{\eta} = \bar{\boldsymbol{\eta}} + M_{\mathscr{S}}(\boldsymbol{x})\tilde{\boldsymbol{\eta}}. \tag{11}$$

The standard variational formulation leads to an expression of the form

$$\int_\Omega \boldsymbol{\nabla}^{\mathrm{s}}\boldsymbol{\eta} : \dot{\boldsymbol{\sigma}}\,\mathrm{d}\Omega = \int_\Omega \boldsymbol{\eta} \cdot \dot{\boldsymbol{f}}\,\mathrm{d}\Omega + \int_\Gamma \boldsymbol{\eta} \cdot \dot{\boldsymbol{t}}\,\mathrm{d}\Gamma. \tag{12}$$

Substituting the weighting function (11) into (12) and using the definition of Dirac delta distribution function yields

$$\int_\Omega [\boldsymbol{\nabla}^{\mathrm{s}}\bar{\boldsymbol{\eta}} + H_{\mathscr{S}}(\boldsymbol{x})\boldsymbol{\nabla}^{\mathrm{s}}\tilde{\boldsymbol{\eta}} - \boldsymbol{\nabla}^{\mathrm{s}}(f^h(\boldsymbol{x})\tilde{\boldsymbol{\eta}})] : \dot{\boldsymbol{\sigma}}\,\mathrm{d}\Omega + \int_{\mathscr{S}} \tilde{\boldsymbol{\eta}} \cdot \dot{\boldsymbol{t}}_{\mathscr{S}}\,\mathrm{d}\Gamma = \int_\Omega (\bar{\boldsymbol{\eta}} + M_{\mathscr{S}}(\boldsymbol{x})\tilde{\boldsymbol{\eta}}) \cdot \dot{\boldsymbol{f}}\,\mathrm{d}\Omega + \int_\Gamma (\bar{\boldsymbol{\eta}} + M_{\mathscr{S}}(\boldsymbol{x})\tilde{\boldsymbol{\eta}}) \cdot \dot{\boldsymbol{t}}\,\mathrm{d}\Gamma, \tag{13}$$

where $\dot{\boldsymbol{t}}_{\mathscr{S}} \equiv \dot{\boldsymbol{t}}_{\mathscr{S}_-}$. Since $\bar{\boldsymbol{\eta}}$ and $\tilde{\boldsymbol{\eta}}$ are two independent weighting functions, we obtain independent variational equations

$$\int_\Omega \boldsymbol{\nabla}^{\mathrm{s}}\bar{\boldsymbol{\eta}} : \dot{\boldsymbol{\sigma}}\,\mathrm{d}\Omega = \int_\Omega \bar{\boldsymbol{\eta}} \cdot \dot{\boldsymbol{f}}\,\mathrm{d}\Omega + \int_\Gamma \bar{\boldsymbol{\eta}} \cdot \dot{\boldsymbol{t}}\,\mathrm{d}\Gamma \tag{14}$$

and

$$\int_\Omega [H_{\mathscr{S}}(\boldsymbol{x})\boldsymbol{\nabla}^{\mathrm{s}}\tilde{\boldsymbol{\eta}} - \boldsymbol{\nabla}^{\mathrm{s}}(f^h(\boldsymbol{x})\tilde{\boldsymbol{\eta}})] : \dot{\boldsymbol{\sigma}}\,\mathrm{d}\Omega + \mathscr{G}_{\mathrm{c}}(\tilde{\boldsymbol{\eta}} \cdot \dot{\boldsymbol{t}}_{\mathscr{S}}) = \int_\Omega M_{\mathscr{S}}(\boldsymbol{x})\tilde{\boldsymbol{\eta}} \cdot \dot{\boldsymbol{f}}\,\mathrm{d}\Omega + \int_\Gamma M_{\mathscr{S}}(\boldsymbol{x})\tilde{\boldsymbol{\eta}} \cdot \dot{\boldsymbol{t}}\,\mathrm{d}\Gamma, \tag{15}$$

where

$$\mathscr{G}_{\mathrm{c}}(\tilde{\boldsymbol{\eta}}, \dot{\boldsymbol{t}}_{\mathscr{S}}) = \int_{\mathscr{S}} \tilde{\boldsymbol{\eta}} \cdot \dot{\boldsymbol{t}}_{\mathscr{S}}\,\mathrm{d}\Gamma \tag{16}$$

is a surface integral arising from slip on the surface of discontinuity. Eq. (14) is the standard variational equation without a discontinuity, whereas (15) is the variational equation associated with the constraint on the discontinuity. Note that the region of integration for (15) is limited to the support of $M_{\mathscr{S}}(\boldsymbol{x})$, as can be seen from the fact that

$$H_{\mathscr{S}}(\boldsymbol{x})\boldsymbol{\nabla}^{\mathrm{s}}\tilde{\boldsymbol{\eta}} - \boldsymbol{\nabla}^{\mathrm{s}}(f^h(\boldsymbol{x})\tilde{\boldsymbol{\eta}}) = M_{\mathscr{S}}(\boldsymbol{x})\boldsymbol{\nabla}^{\mathrm{s}}\tilde{\boldsymbol{\eta}} - (\tilde{\boldsymbol{\eta}} \otimes \boldsymbol{\nabla} f^h(\boldsymbol{x}))^{\mathrm{s}}. \tag{17}$$

Since $f^h(\boldsymbol{x}) = 0, 1$ outside of the support Ω^h, the above expression vanishes in $\Omega \setminus \Omega^h$.

3. Galerkin approximation and matrix equations

Using the standard Galerkin approximation in which the trial and weighting functions are the same, we develop matrix equations consistent with the variational equations of the previous section.

3.1. Rate form

For any element Ω^e containing a crack the continuous part of the velocity field is approximated by standard C^0 shape functions $N^e_I(\boldsymbol{x})$

$$\bar{\boldsymbol{v}}(\boldsymbol{x}) = \sum_{I \in N_{\mathrm{en}}} N^e_I(\boldsymbol{x})\dot{\boldsymbol{d}}^e_I = \boldsymbol{N}^e\dot{\boldsymbol{d}}^e, \quad \boldsymbol{x} \in \Omega^e, \tag{18}$$

where $\dot{\boldsymbol{d}}^e_I$ is the regular nodal velocity vector and N_{en} is the set of regular nodes for element Ω^e, represented as dark circles in Fig. 2. The velocity field $\tilde{\boldsymbol{v}}$ is approximated by shape

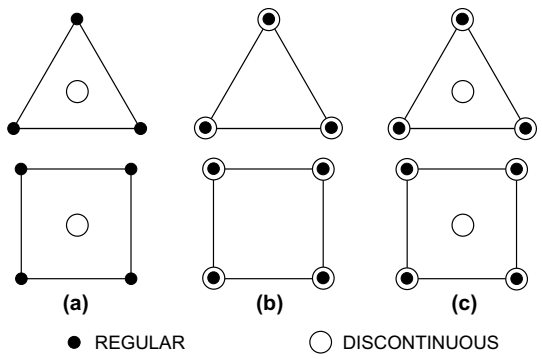

Fig. 2. Mixed finite elements for resolving a crack: (a) subinterpolated discontinuous velocity field employed by the assumed enhanced strains method; (b) isointerpolated discontinuous velocity field employed by the extended finite element method; (c) superinterpolated discontinuous velocity field.

functions $\mathscr{N}^e_I(\boldsymbol{x})$, which are not necessarily the same as $N^e_I(\boldsymbol{x})$

$$\tilde{\boldsymbol{v}}(\boldsymbol{x}) = \sum_{I\in N'_{\text{en}}} \mathscr{N}^e_I(\boldsymbol{x})\dot{\boldsymbol{a}}^e_I = \mathscr{N}^e\dot{\boldsymbol{a}}^e, \qquad \boldsymbol{x}\in\Omega^e, \tag{19}$$

where $\dot{\boldsymbol{a}}^e_I$ is the vector of element nodal enhancements and N'_{en} is the set of enhancement nodes for element Ω^e, represented as white circles in Fig. 2. The enhanced finite elements shown in Fig. 2 are similar to those used in a mixed variational formulation [71] in that a node may contain two types of degrees of freedom. We will consider specific forms for the shape function matrix $\mathscr{N}^e$ in the next section.

The velocity field $f^h(\boldsymbol{x})\tilde{\boldsymbol{v}}(\boldsymbol{x})$ is interpolated according to the expression

$$f^h(\boldsymbol{x})\tilde{\boldsymbol{v}}(\boldsymbol{x}) = \sum_{I\in N'_{\text{en}}} \widetilde{\mathscr{N}}^e_I(\boldsymbol{x})\dot{\boldsymbol{a}}^e_I = \widetilde{\mathscr{N}}^e\dot{\boldsymbol{a}}^e, \quad \boldsymbol{x}\in\Omega^e, \tag{20}$$

where $\widetilde{\mathscr{N}}^e$ is a shape function matrix chosen to satisfy the requirements spelled out in (4). Specific forms for this matrix will also be presented in the next section. The discontinuous part of velocity field then takes the form

$$M_{\mathscr{S}}(\boldsymbol{x})\tilde{\boldsymbol{v}}(\boldsymbol{x}) = \sum_{I\in N'_{\text{en}}} \widetilde{N}^e_I(\boldsymbol{x})\dot{\boldsymbol{a}}^e_I = \widetilde{\boldsymbol{N}}^e\dot{\boldsymbol{a}}^e, \quad \boldsymbol{x}\in\Omega^e, \tag{21}$$

where

$$\widetilde{N}^e_I(\boldsymbol{x}) = \mathscr{N}^e_I(\boldsymbol{x})H_{\mathscr{S}}(\boldsymbol{x}) - \widetilde{\mathscr{N}}^e_I(\boldsymbol{x}). \tag{22}$$

Thus, the total velocity field becomes

$$\boldsymbol{v}(\boldsymbol{x}) = \boldsymbol{N}^e\dot{\boldsymbol{d}}^e + \widetilde{\boldsymbol{N}}^e\dot{\boldsymbol{a}}^e, \quad \boldsymbol{x}\in\Omega^e. \tag{23}$$

We see that the contributions of $\dot{\boldsymbol{a}}^e$ at the regular nodes are zero from the use of the blending function, so $\dot{\boldsymbol{d}}^e$ represents the total velocity vector at the regular nodes. Accordingly, the strain rate vector is

$$\dot{\boldsymbol{\epsilon}}(\boldsymbol{x}) = \boldsymbol{B}^e\dot{\boldsymbol{d}}^e + \widetilde{\boldsymbol{B}}^e\dot{\boldsymbol{a}}^e, \quad \boldsymbol{x}\in\Omega^e\setminus\mathscr{S}^e, \tag{24}$$

where $\boldsymbol{B}^e = \nabla^{\text{s}}\boldsymbol{N}^e$ and $\widetilde{\boldsymbol{B}}^e = \nabla^{\text{s}}\widetilde{\boldsymbol{N}}^e$. The velocity jump on $\mathscr{S}$ is

$$[\![\boldsymbol{v}(\boldsymbol{x}_{\mathscr{S}})]\!] = \tilde{\boldsymbol{v}}(\boldsymbol{x}_{\mathscr{S}}) = \mathscr{N}^e|_{\boldsymbol{x}_{\mathscr{S}}}\dot{\boldsymbol{a}}^e \tag{25}$$

with a slight abuse in notation by denoting the strain rate tensor and vector with the same symbol.

Employing the standard Galerkin approximation in which the trial and weighting functions are interpolated in a similar fashion, the global finite element matrix equation consistent with variational Eq. (14) is

$$\dot{\boldsymbol{F}}_{\text{INT}}(\dot{\boldsymbol{d}},\dot{\boldsymbol{a}}) = \dot{\boldsymbol{F}}_{\text{EXT}}, \tag{26}$$

where

$$\begin{aligned}\dot{\boldsymbol{F}}_{\text{INT}} &= \int_\Omega \boldsymbol{B}^{\text{T}}\dot{\boldsymbol{\sigma}}\,\text{d}\Omega,\\ \dot{\boldsymbol{F}}_{\text{EXT}} &= \int_\Omega \boldsymbol{N}^{\text{T}}\dot{\boldsymbol{f}}\,\text{d}\Omega + \int_\Gamma \boldsymbol{N}^{\text{T}}\dot{\boldsymbol{t}}\,\text{d}\Gamma.\end{aligned} \tag{27}$$

Implied in (26) is that the stress rate $\dot{\boldsymbol{\sigma}}$ depends on $\dot{\boldsymbol{d}}$ and $\dot{\boldsymbol{a}}$ through the strain rate $\dot{\boldsymbol{\epsilon}}$.

The global finite element matrix equation consistent with (15) is

$$\dot{\mathscr{F}}_{\text{INT}}(\dot{\boldsymbol{d}},\dot{\boldsymbol{a}}) + \dot{\mathscr{G}}_{\text{INT}}(\dot{\boldsymbol{a}}) = \dot{\mathscr{F}}_{\text{EXT}}, \tag{28}$$

where

$$\begin{aligned}\dot{\mathscr{F}}_{\text{INT}} &= \int_{\Omega^h\setminus\mathscr{S}} \widetilde{\boldsymbol{B}}^{\text{T}}\dot{\boldsymbol{\sigma}}\,\text{d}\Omega,\\ \dot{\mathscr{G}}_{\text{INT}} &= \int_{\mathscr{S}} \mathscr{N}^{\text{T}}\dot{\boldsymbol{t}}_{\mathscr{S}}\,\text{d}\mathscr{S},\\ \dot{\mathscr{F}}_{\text{EXT}} &= \int_{\Omega^h} \widetilde{\boldsymbol{N}}^{\text{T}}\dot{\boldsymbol{f}}\,\text{d}\Omega + \int_{\Gamma^h} \widetilde{\boldsymbol{N}}^{\text{T}}\dot{\boldsymbol{t}}\,\text{d}\Gamma.\end{aligned} \tag{29}$$

Implied in (28) is that the traction rate vector $\dot{\boldsymbol{t}}_{\mathscr{S}}$ depends solely on the velocity jump via (25), but not on the regular displacements. Note that $\dot{\mathscr{F}}_{\text{EXT}}$ and $\dot{\mathscr{F}}_{\text{INT}}$ use the enhanced shape function matrix $\widetilde{\boldsymbol{N}}$, whereas $\dot{\mathscr{G}}_{\text{INT}}$ uses the shape function matrix $\mathscr{N}$.

To further elucidate the matrix equations, consider tangential constitutive equations of the form

$$\dot{\boldsymbol{\sigma}}(\boldsymbol{x}) = \boldsymbol{D}(\boldsymbol{x})\dot{\boldsymbol{\epsilon}}(\boldsymbol{x}), \quad \dot{\boldsymbol{t}}_{\mathscr{S}}(\boldsymbol{x}_{\mathscr{S}}) = \boldsymbol{E}(\boldsymbol{x}_{\mathscr{S}})\tilde{\boldsymbol{v}}(\boldsymbol{x}_{\mathscr{S}}), \tag{30}$$

where $\boldsymbol{D}$ and $\boldsymbol{E}$ are tangent stiffness matrices that could vary with the state of stress. The coupled matrix equations (26) and (28) then reduce to the more compact form

$$\begin{bmatrix}\boldsymbol{A}_{11} & \boldsymbol{A}_{12}\\ \boldsymbol{A}_{21} & \boldsymbol{A}_{22}\end{bmatrix}\begin{Bmatrix}\dot{\boldsymbol{d}}\\ \dot{\boldsymbol{a}}\end{Bmatrix} = \begin{Bmatrix}\dot{\boldsymbol{F}}_{\text{EXT}}\\ \dot{\mathscr{F}}_{\text{EXT}}\end{Bmatrix}, \tag{31}$$

where

$$\begin{aligned}\boldsymbol{A}_{11} &= \int_\Omega \boldsymbol{B}^{\text{T}}\boldsymbol{D}\boldsymbol{B}\,\text{d}\Omega, \quad \boldsymbol{A}_{12} = \int_\Omega \boldsymbol{B}^{\text{T}}\boldsymbol{D}\widetilde{\boldsymbol{B}}\,\text{d}\Omega,\\ \boldsymbol{A}_{21} &= \int_{\Omega^h} \widetilde{\boldsymbol{B}}^{\text{T}}\boldsymbol{D}\boldsymbol{B}\,\text{d}\Omega, \quad \boldsymbol{A}_{22} = \overline{\boldsymbol{A}}_{22} + \overline{\overline{\boldsymbol{A}}}_{22},\\ \overline{\boldsymbol{A}}_{22} &= \int_{\Omega^h} \widetilde{\boldsymbol{B}}^{\text{T}}\boldsymbol{D}\widetilde{\boldsymbol{B}}\,\text{d}\Omega, \quad \overline{\overline{\boldsymbol{A}}}_{22} = \int_{\mathscr{S}} \mathscr{N}^{\text{T}}\boldsymbol{E}\mathscr{N}\,\text{d}\mathscr{S}.\end{aligned} \tag{32}$$

The Galerkin approximation yields a symmetric system for symmetric constitutive matrices $\boldsymbol{D}$ and $\boldsymbol{E}$.

3.2. Time-integrated form

The time-integrated global matrix equation is of the form

$$\boldsymbol{F}_{\mathrm{INT}}(\boldsymbol{d},\boldsymbol{a}) = \boldsymbol{F}_{\mathrm{EXT}}, \tag{33}$$

where

$$\begin{aligned}\boldsymbol{F}_{\mathrm{INT}} &= \int_{\Omega} \boldsymbol{B}^{\mathrm{T}}\boldsymbol{\sigma}\,\mathrm{d}\Omega,\\ \boldsymbol{F}_{\mathrm{EXT}} &= \int_{\Omega} \boldsymbol{N}^{\mathrm{T}}\boldsymbol{f}\,\mathrm{d}\Omega + \int_{\Gamma} \boldsymbol{N}^{\mathrm{T}}\boldsymbol{t}\,\mathrm{d}\Gamma.\end{aligned} \tag{34}$$

The above equations are augmented by the time-integrated enhancement equations

$$\mathscr{F}_{\mathrm{INT}}(\boldsymbol{d},\boldsymbol{a}) + \mathscr{G}_{\mathrm{INT}}(\boldsymbol{a}) = \mathscr{F}_{\mathrm{EXT}}, \tag{35}$$

where

$$\begin{aligned}\mathscr{F}_{\mathrm{INT}} &= \int_{\Omega^h\setminus\mathscr{S}} \widetilde{\boldsymbol{B}}^{\mathrm{T}}\boldsymbol{\sigma}\,\mathrm{d}\Omega,\\ \mathscr{G}_{\mathrm{INT}} &= \int_{\mathscr{S}} \mathscr{N}^{\mathrm{T}}\boldsymbol{t}_{\mathscr{S}}\,\mathrm{d}\mathscr{S},\\ \mathscr{F}_{\mathrm{EXT}} &= \int_{\Omega^h} \widetilde{\boldsymbol{N}}^{\mathrm{T}}\boldsymbol{f}\,\mathrm{d}\Omega + \int_{\Gamma^h} \widetilde{\boldsymbol{N}}^{\mathrm{T}}\boldsymbol{t}\,\mathrm{d}\Gamma.\end{aligned} \tag{36}$$

The matrix equations are best solved in residual form

$$\mathscr{D} = \begin{Bmatrix}\boldsymbol{d}\\ \boldsymbol{a}\end{Bmatrix}, \quad \boldsymbol{r}(\mathscr{D}) = \begin{Bmatrix}\boldsymbol{F}_{\mathrm{EXT}} - \boldsymbol{F}_{\mathrm{INT}}\\ \mathscr{F}_{\mathrm{EXT}} - \mathscr{F}_{\mathrm{INT}} - \mathscr{G}_{\mathrm{INT}}\end{Bmatrix}. \tag{37}$$

We thus want a solution vector $\mathscr{D}^*$ such that $\boldsymbol{r}(\mathscr{D}^*) = \boldsymbol{0}$. Solving with Newton's method requires an evaluation of the algorithmic tangent operator

$$-\boldsymbol{r}'(\mathscr{D}^k) = \begin{bmatrix}\boldsymbol{A}_{11} & \boldsymbol{A}_{12}\\ \boldsymbol{A}_{21} & \boldsymbol{A}_{22}\end{bmatrix}^k, \tag{38}$$

where k denotes an iteration counter, and

$$\begin{aligned}\boldsymbol{A}_{11} &= \int_{\Omega} \boldsymbol{B}^{\mathrm{T}}\boldsymbol{D}^k\boldsymbol{B}\,\mathrm{d}\Omega, \quad \boldsymbol{A}_{12} = \int_{\Omega} \boldsymbol{B}^{\mathrm{T}}\boldsymbol{D}^k\widetilde{\boldsymbol{B}}\,\mathrm{d}\Omega,\\ \boldsymbol{A}_{21} &= \int_{\Omega^h} \widetilde{\boldsymbol{B}}^{\mathrm{T}}\boldsymbol{D}^k\boldsymbol{B}\,\mathrm{d}\Omega, \quad \boldsymbol{A}_{22} = \overline{\boldsymbol{A}}_{22} + \overline{\overline{\boldsymbol{A}}}_{22},\\ \overline{\boldsymbol{A}}_{22} &= \int_{\Omega^h} \widetilde{\boldsymbol{B}}^{\mathrm{T}}\boldsymbol{D}^k\widetilde{\boldsymbol{B}}\,\mathrm{d}\Omega, \quad \overline{\overline{\boldsymbol{A}}}_{22} = \int_{\mathscr{S}} \mathscr{N}^{\mathrm{T}}\boldsymbol{E}^k\mathscr{N}\,\mathrm{d}\mathscr{S}.\end{aligned} \tag{39}$$

In implementing the above iterative algorithm, it is assumed that there exist constitutive evolution equations (again, with a slight abuse in notation by denoting the stress and strain vectors and tensors with the same symbol)

$$\boldsymbol{\sigma} = \boldsymbol{\sigma}(\boldsymbol{\epsilon}), \quad \boldsymbol{t}_{\mathscr{S}} = \boldsymbol{t}_{\mathscr{S}}(\widetilde{\boldsymbol{u}}), \tag{40}$$

so that

$$\boldsymbol{D}^k = \left.\frac{\partial\boldsymbol{\sigma}}{\partial\boldsymbol{\epsilon}}\right|^k, \quad \boldsymbol{E}^k = \left.\frac{\partial\boldsymbol{t}_{\mathscr{S}}}{\partial\widetilde{\boldsymbol{u}}}\right|^k, \tag{41}$$

where $\dot{\widetilde{\boldsymbol{u}}} \equiv \tilde{\boldsymbol{v}}$. In other words, the constitutive tangent operators $\boldsymbol{D}$ and $\boldsymbol{E}$ are simply replaced by their respective algorithmic values, $\boldsymbol{D}^k$ and $\boldsymbol{E}^k$, at iteration k. Two constitutive evolution laws are therefore needed to drive the solution: (a) the continuum constitutive law for the bulk solid, and (b) the interface constitutive law for the crack.

4. Specializations of the matrix equations

Depending on the choice of interpolation functions we could recover a number of different element enhancement techniques.

4.1. The extended finite element method

The extended finite element method is the most recognizable member of the above family of Galerkin techniques and employs the same interpolation for $\bar{\boldsymbol{v}}$ and $\tilde{\boldsymbol{v}}$ (isointerpolation). For any enhanced element Ω^e we have

$$\bar{\boldsymbol{v}}(\boldsymbol{x}) = \boldsymbol{N}^e\dot{\boldsymbol{d}}^e, \quad \tilde{\boldsymbol{v}}(\boldsymbol{x}) = \mathscr{N}^e\dot{\boldsymbol{a}}^e, \quad \boldsymbol{N}^e = \mathscr{N}^e, \tag{42}$$

for all $\boldsymbol{x} \in \Omega^e$. A natural choice is to set $N_{\mathrm{en}} = N'_{\mathrm{en}}$, so no additional nodes are introduced and the regular nodes of Ω^e are simply enhanced. Each enhanced node of Ω^e then contains a total number of $2n_{\mathrm{reg}}$ degrees of freedom, where n_{reg} = number of regular degrees of freedom for each node, see Fig. 2.

The velocity field $f^h(\boldsymbol{x})\tilde{\boldsymbol{v}}(\boldsymbol{x})$ in an enhanced finite element Ω^e may be interpolated according to the equation

$$f^h(\boldsymbol{x})\tilde{\boldsymbol{v}}(\boldsymbol{x}) = \sum_{I\in N_{\mathrm{en}}} N_I^e(\boldsymbol{x})H_{\mathscr{S}}(\boldsymbol{x}_I)\dot{\boldsymbol{a}}_I^e \equiv \sum_{I\in N_{\mathrm{en}}} \widetilde{\mathscr{N}}_I^e(\boldsymbol{x})\dot{\boldsymbol{a}}_I^e. \tag{43}$$

Hence,

$$\widetilde{\mathscr{N}}_I^e(\boldsymbol{x}) = N_I^e(\boldsymbol{x})H_{\mathscr{S}}(\boldsymbol{x}_I), \quad I \in N_{\mathrm{en}}. \tag{44}$$

The discontinuous part of the velocity field takes the form

$$\begin{aligned}M_{\mathscr{S}}(\boldsymbol{x})\tilde{\boldsymbol{v}}(\boldsymbol{x}) &= \sum_{I\in N_{\mathrm{en}}} N_I^e(\boldsymbol{x})[H_{\mathscr{S}}(\boldsymbol{x}) - H_{\mathscr{S}}(\boldsymbol{x}_I)]\dot{\boldsymbol{a}}_I^e\\ &\equiv \sum_{I\in N_{\mathrm{en}}} \widetilde{N}_I^e(\boldsymbol{x})\dot{\boldsymbol{a}}_I^e.\end{aligned} \tag{45}$$

Hence,

$$\widetilde{N}_I^e(\boldsymbol{x}) = N_I^e(\boldsymbol{x})[H_{\mathscr{S}}(\boldsymbol{x}) - H_{\mathscr{S}}(\boldsymbol{x}_I)]. \tag{46}$$

Finally, the velocity jump on $\mathscr{S}$ is given by

$$\tilde{\boldsymbol{v}}(\boldsymbol{x}_{\mathscr{S}}) = \sum_{I\in N_{\mathrm{en}}} N_I^e(\boldsymbol{x}_{\mathscr{S}})\dot{\boldsymbol{a}}_I^e = \boldsymbol{N}^e|_{\boldsymbol{x}_{\mathscr{S}}}\dot{\boldsymbol{a}}^e. \tag{47}$$

For the extended finite element method employing CST elements the functions $f^h(\boldsymbol{x})\tilde{\boldsymbol{v}}(\boldsymbol{x})$ and $M_{\mathscr{S}}(\boldsymbol{x})\tilde{\boldsymbol{v}}(\boldsymbol{x})$ are shown in Fig. 3.

4.2. One-node (reduced) interpolation of discontinuous velocity

Consider an enhanced finite element Ω^e with a regular C_0-continuous interpolation of $\bar{\boldsymbol{v}}$ and a one-node interpolation of $\tilde{\boldsymbol{v}}$. Because $\tilde{\boldsymbol{v}}(\boldsymbol{x})$ is piecewise constant, it is discontinuous across the element boundaries, see Fig. 2. Setting $N'_{\mathrm{en}} = 1$ and $\mathscr{N}_1^e(\boldsymbol{x}) \equiv 1$ for all $\boldsymbol{x} \in \Omega^e$, we get

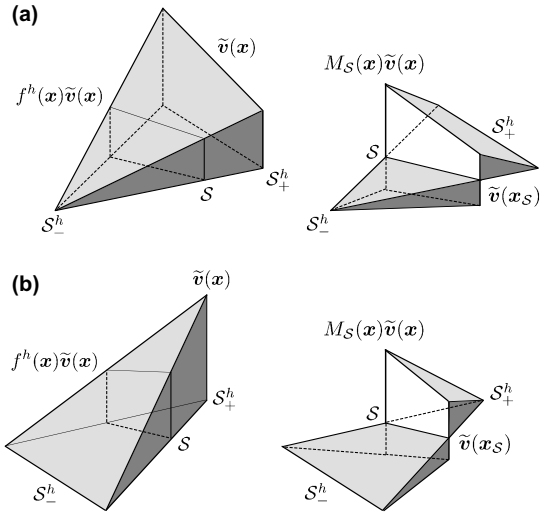

Fig. 3. Plots of blending velocity $f^h(\boldsymbol{x})\tilde{\boldsymbol{v}}(\boldsymbol{x})$ and discontinuous velocity $M_{\mathscr{S}}(\boldsymbol{x})\tilde{\boldsymbol{v}}(\boldsymbol{x})$ for an enhanced CST element with the extended finite element method: (a) two nodes on the positive side of $\mathscr{S}$; (b) one node on the positive side of $\mathscr{S}$. The velocity jump $\tilde{\boldsymbol{v}}(\boldsymbol{x}_{\mathscr{S}})$ is interpolated linearly on $\mathscr{S}$.

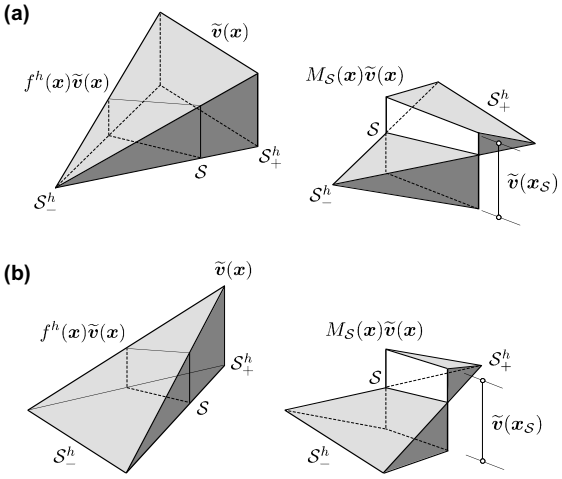

Fig. 4. Plots of blending velocity $f^h(\boldsymbol{x})\tilde{\boldsymbol{v}}(\boldsymbol{x})$ and discontinuous velocity $M_{\mathscr{S}}(\boldsymbol{x})\tilde{\boldsymbol{v}}(\boldsymbol{x})$ for an enhanced CST element with a one-node discontinuous velocity interpolation: (a) two nodes on the positive side of $\mathscr{S}$; (b) one node on the positive side of $\mathscr{S}$. The velocity jump $\tilde{\boldsymbol{v}}(\boldsymbol{x}_{\mathscr{S}})$ is piecewise constant on $\mathscr{S}$.

$$\tilde{\boldsymbol{v}}(\boldsymbol{x}) = \dot{\boldsymbol{a}}_1^e = \text{constant}, \quad \boldsymbol{x} \in \Omega^e. \tag{48}$$

The blending velocity takes the form

$$f^h(\boldsymbol{x})\tilde{\boldsymbol{v}}(\boldsymbol{x}) = \left[\sum_{J\in N_{\text{en}}} N_J^e(\boldsymbol{x}) H_{\mathscr{S}}(\boldsymbol{x}_J)\right]\dot{\boldsymbol{a}}_1^e \equiv \widetilde{\mathscr{N}}_1^e(\boldsymbol{x})\dot{\boldsymbol{a}}_1^e. \tag{49}$$

Thus,

$$\widetilde{\mathscr{N}}_1^e(\boldsymbol{x}) = \sum_{J\in N_{\text{en}}} N_J^e(\boldsymbol{x}) H_{\mathscr{S}}(\boldsymbol{x}_J). \tag{50}$$

The discontinuous part of velocity is given by

$$\begin{aligned} M_{\mathscr{S}}(\boldsymbol{x})\tilde{\boldsymbol{v}}(\boldsymbol{x}) &= \left[H_{\mathscr{S}}(\boldsymbol{x}) - \sum_{J\in N_{\text{en}}} N_J^e(\boldsymbol{x}) H_{\mathscr{S}}(\boldsymbol{x}_J)\right]\dot{\boldsymbol{a}}_1^e \\ &= \widetilde{N}_1^e(\boldsymbol{x})\dot{\boldsymbol{a}}_1^e. \end{aligned} \tag{51}$$

Therefore,

$$\widetilde{N}_1^e(\boldsymbol{x}) = H_{\mathscr{S}}(\boldsymbol{x}) - \sum_{J\in N_{\text{en}}} N_J^e(\boldsymbol{x}) H_{\mathscr{S}}(\boldsymbol{x}_J). \tag{52}$$

Finally, the velocity jump on $\mathscr{S}$ is given by the function

$$\tilde{\boldsymbol{v}}(\boldsymbol{x}_{\mathscr{S}}) = \dot{\boldsymbol{a}}_1^e \equiv \dot{\zeta}^e \boldsymbol{m}^e, \tag{53}$$

where $\dot{\zeta}^e$ is the slip rate with instantaneous unit direction $\boldsymbol{m}^e$. Fig. 4 shows the functions $f^h(\boldsymbol{x})\tilde{\boldsymbol{v}}(\boldsymbol{x})$ and $M_{\mathscr{S}}(\boldsymbol{x})\tilde{\boldsymbol{v}}(\boldsymbol{x})$ for a 2D CST element with a one-node interpolation of discontinuous velocity.

For this reduced interpolation of discontinuous velocity the Galerkin approximations imposed over an enhanced element Ω^e consistent with variational equations (14) and (15) are given by the pair of expressions

$$\int_{\Omega^e} \nabla^{\text{s}}\bar{\boldsymbol{\eta}}^h : \dot{\boldsymbol{\sigma}}\,\mathrm{d}\Omega = \int_{\Omega^e} \bar{\boldsymbol{\eta}}^h \cdot \dot{\boldsymbol{f}}\,\mathrm{d}\Omega + \int_{\Gamma^e} \bar{\boldsymbol{\eta}}^h \cdot \dot{\boldsymbol{t}}\,\mathrm{d}\Gamma \tag{54}$$

and

$$\int_{\Omega^e} \tilde{\boldsymbol{\varphi}}^h : \dot{\boldsymbol{\sigma}}\,\mathrm{d}\Omega = \int_{\Omega^e} M_{\mathscr{S}}(\boldsymbol{x})\boldsymbol{m}^e \cdot \dot{\boldsymbol{f}}\,\mathrm{d}\Omega + \int_{\Gamma^e} M_{\mathscr{S}}(\boldsymbol{x})\boldsymbol{m}^e \cdot \dot{\boldsymbol{t}}\,\mathrm{d}\Gamma, \tag{55}$$

where

$$\tilde{\boldsymbol{\varphi}}^h = -(\boldsymbol{m}^e \otimes \nabla f^h(\boldsymbol{x}))^{\text{s}} + (\boldsymbol{m}^e \otimes \boldsymbol{n}^e)^{\text{s}}\delta_{\mathscr{S}}. \tag{56}$$

The element matrix equations are given by

$$\begin{bmatrix} \boldsymbol{A}_{11}^e & \boldsymbol{A}_{12}^e \\ \boldsymbol{A}_{21}^e & A_{22}^e \end{bmatrix} \begin{Bmatrix} \dot{\boldsymbol{d}}^e \\ \dot{\zeta}^e \end{Bmatrix} = \begin{Bmatrix} \dot{\boldsymbol{F}}_{\text{ext}}^e \\ \dot{\mathscr{F}}_{\text{ext}}^e \end{Bmatrix}, \tag{57}$$

where

$$\begin{aligned} \boldsymbol{A}_{11}^e &= \int_{\Omega^e} \boldsymbol{B}^{\text{T}}\boldsymbol{D}\boldsymbol{B}\,\mathrm{d}\Omega, \quad \boldsymbol{A}_{12}^e = -\int_{\Omega^e} \boldsymbol{B}^{\text{T}}\boldsymbol{D}\boldsymbol{\beta}\,\mathrm{d}\Omega, \\ \boldsymbol{A}_{21}^e &= -\int_{\Omega^e} \boldsymbol{\beta}^{\text{T}}\boldsymbol{D}\boldsymbol{B}\,\mathrm{d}\Omega, \\ A_{22}^e &= \int_{\Omega^e} \boldsymbol{\beta}^{\text{T}}\boldsymbol{D}\boldsymbol{\beta}\,\mathrm{d}\Omega + \int_{\mathscr{S}^e} \boldsymbol{m}^{eT}\boldsymbol{E}\boldsymbol{m}^e\,\mathrm{d}\mathscr{S} \end{aligned} \tag{58}$$

and

$$\begin{aligned} \dot{\boldsymbol{F}}_{\text{ext}}^e &= \int_{\Omega^e} \boldsymbol{N}^{\text{T}}\dot{\boldsymbol{f}}\,\mathrm{d}\Omega + \int_{\Gamma^e} \boldsymbol{N}^{\text{T}}\dot{\boldsymbol{t}}\,\mathrm{d}\Gamma, \\ \dot{\mathscr{F}}_{\text{ext}}^e &= \int_{\Omega^e} M_{\mathscr{S}}(\boldsymbol{x})\boldsymbol{m}^e \cdot \dot{\boldsymbol{f}}\,\mathrm{d}\Omega + \int_{\Gamma^e} M_{\mathscr{S}}(\boldsymbol{x})\boldsymbol{m}^e \cdot \dot{\boldsymbol{t}}\,\mathrm{d}\Gamma \end{aligned} \tag{59}$$

and where the column vector $\boldsymbol{\beta}$ is assembled from the tensor $(\boldsymbol{m}^e \otimes \nabla f^h(\boldsymbol{x}))^{\text{s}}$.

4.3. A superinterpolated discontinuous velocity

Consider the following interpolation

$$\bar{\boldsymbol{v}}(\boldsymbol{x}) = \sum_{I\in N_{\text{en}}} N_I^e(\boldsymbol{x})\dot{\boldsymbol{d}}_I^e, \quad \tilde{\boldsymbol{v}}(\boldsymbol{x}) = \sum_{I\in (N_{\text{en}}\cup B)} \mathscr{N}_I^e(\boldsymbol{x})\dot{\boldsymbol{a}}_I^e, \tag{60}$$

where $N_I^e(\boldsymbol{x})$ is the standard shape function for the regular degree of freedom, B is a bubble node, and $N_{\text{en}} \cup B \equiv N'_{\text{en}}$, see Fig. 2c. The shape functions $\mathscr{N}_I^e(\boldsymbol{x})$ are derived from $N_I^e(\boldsymbol{x})$ so that $\mathscr{N}_I^e(\boldsymbol{x}_J) = \delta_{IJ}$ for any nodes $I,J \in (N_{\text{en}} \cup B)$. More specifically, for a four-node quadrilateral element the shape functions in terms of natural coordinates ξ and η are

$$\mathscr{N}_B^e(\xi,\eta) = (1-\xi^2)(1-\eta^2) \tag{61}$$

for the bubble node, and

$$\mathscr{N}_I^e(\xi,\eta) = \frac{1}{4}(1+\xi_I\xi)(1+\eta_I\eta) - \frac{1}{4}\mathscr{N}_B^e(\xi,\eta) \tag{62}$$

for the corner nodes, where $\xi_I, \eta_I = \pm 1$ define the natural coordinates of the corner nodes. As noted in the Introduction, a higher order interpolation for discontinuous velocity may be beneficial for the treatment of more complex contact cohesive–frictional laws.

The velocity field $f^h(\boldsymbol{x})\tilde{\boldsymbol{v}}(\boldsymbol{x})$ may be interpolated with or without the bubble node. Recall that this function only needs to satisfy restrictions (4), so its interpolation may not be unique. With the bubble node, the interpolation takes the form

$$f^h(\boldsymbol{x})\tilde{\boldsymbol{v}}(\boldsymbol{x}) = \sum_{I\in N_{\text{en}}} \mathscr{N}_I^e(\boldsymbol{x}) H_{\mathscr{S}}(\boldsymbol{x}_I)\dot{\boldsymbol{a}}_I^e + \mathscr{N}_B^e(\boldsymbol{x})\dot{\boldsymbol{a}}_B^e. \tag{63}$$

Without the bubble node, the interpolation reduces to that used in the extended finite element method,

$$f^h(\boldsymbol{x})\tilde{\boldsymbol{v}}(\boldsymbol{x}) = \sum_{I\in N_{\text{en}}} N_I^e(\boldsymbol{x}) H_{\mathscr{S}}(\boldsymbol{x}_I)\dot{\boldsymbol{a}}_I^e. \tag{64}$$

The discontinuous part of velocity reflects the presence of the bubble node. Using (64) along with the Heaviside function, we get

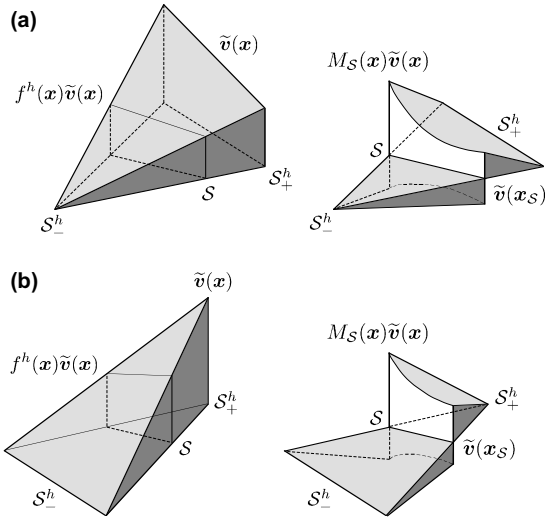

Fig. 5. Plots of blending velocity $f^h(\boldsymbol{x})\tilde{\boldsymbol{v}}(\boldsymbol{x})$ and discontinuous velocity $M_{\mathscr{S}}(\boldsymbol{x})\tilde{\boldsymbol{v}}(\boldsymbol{x})$ for an enhanced CST element with a superinterpolated discontinuous velocity field: (a) two nodes on the positive side of $\mathscr{S}$; (b) one node on the positive side of $\mathscr{S}$. The velocity jump $\tilde{\boldsymbol{v}}(\boldsymbol{x}_{\mathscr{S}})$ is quadratic on $\mathscr{S}$.

$$M_{\mathscr{S}}(\boldsymbol{x})\tilde{\boldsymbol{v}}(\boldsymbol{x}) = \sum_{I\in N_{\text{en}}} [\mathscr{N}_I^e(\boldsymbol{x}) H_{\mathscr{S}}(\boldsymbol{x}) - N_I^e(\boldsymbol{x}) H_{\mathscr{S}}(\boldsymbol{x}_I)]\dot{\boldsymbol{a}}_I^e + \mathscr{N}_B^e(\boldsymbol{x}) H_{\mathscr{S}}(\boldsymbol{x})\dot{\boldsymbol{a}}_B^e. \tag{65}$$

In this case the velocity jump on $\mathscr{S}$ is

$$\tilde{\boldsymbol{v}}(\boldsymbol{x}_{\mathscr{S}}) = \sum_{I\in(N_{\text{en}}\cup B)} \mathscr{N}_I^e(\boldsymbol{x}_{\mathscr{S}})\dot{\boldsymbol{a}}_I^e. \tag{66}$$

For a CST element, introduction of a bubble node results in a curvilinear interpolation of velocity jump within the element, as shown in Fig. 5. As to the efficacy of this interpolation, the author is not aware of any previous work where a bubble node has been introduced in the above context. However, this technique could prove beneficial when dealing with far more complex cohesive–frictional laws, such as the rate- and state-dependent frictional laws involving both spatial and temporal variations of the coefficient of friction, see [14].

5. The AES method

The assumed enhanced strain (AES) method involves local enrichments that in some way resemble the one-node interpolation described in Section 4.2 except that the weighting function is designed to pass the patch test requiring a zero element mean. The AES method is often associated with "static condensation" since the local nature of the enhancement permits its elimination on the element level. For CST elements the Galerkin embedded discontinuity method is an alternative formulation to the AES method in that slip is treated as a plastic multiplier of continuum plasticity, thereby completely avoiding the extra step of static condensation in the element matrix assembly.

5.1. Petrov–Galerkin formulation

We revisit equation (1) and once again use a piecewise constant interpolation for $\tilde{\boldsymbol{v}}$. The associated strain field is

$$\nabla^{\text{s}}\boldsymbol{v}(\boldsymbol{x}) = \nabla^{\text{s}}\bar{\boldsymbol{v}}(\boldsymbol{x}) + (\tilde{\boldsymbol{v}}(\boldsymbol{x}) \otimes \nabla M_{\mathscr{S}}(\boldsymbol{x}))^{\text{s}}, \tag{67}$$

where

$$\nabla M_{\mathscr{S}}(\boldsymbol{x}) = \boldsymbol{n}^e\delta_{\mathscr{S}} - \nabla f^h(\boldsymbol{x}). \tag{68}$$

Now, for all $\boldsymbol{x} \in \Omega^h \setminus \mathscr{S}^e$ the strain rate tensor is

$$\dot{\boldsymbol{\epsilon}}(\boldsymbol{x}) = \underbrace{\dot{\bar{\boldsymbol{\epsilon}}}(\boldsymbol{x})}_{\text{regular}} + \underbrace{\dot{\tilde{\boldsymbol{\epsilon}}}(\boldsymbol{x})}_{\text{enhanced}}, \quad \dot{\tilde{\boldsymbol{\epsilon}}}(\boldsymbol{x}) = -(\nabla f^h(\boldsymbol{x}) \otimes \tilde{\boldsymbol{v}}(\boldsymbol{x}))^{\text{s}}. \tag{69}$$

This leads to the following field of trial functions for the enhanced strain rates:

$$\tilde{\mathscr{E}}^h = \{\dot{\tilde{\boldsymbol{\epsilon}}}^h \in (H^0)^6 | \dot{\tilde{\boldsymbol{\epsilon}}}^h = -(\tilde{\boldsymbol{v}}(\boldsymbol{x}) \otimes \nabla f^h(\boldsymbol{x}))^{\text{s}}\}. \tag{70}$$

Note that this set of trial functions is the same as that employed in Section 4.2.

In the AES method the field of weighting functions for the enhanced strain rates is derived "by construction". The specific field of enhanced weighting functions proposed in [30] is given by

$$\widetilde{\mathscr{G}}^h = \{\tilde{\gamma}^h \in (H^0)^6 | \tilde{\gamma}^h = (-C + \delta_{\mathscr{S}})(\boldsymbol{m}^e \otimes \boldsymbol{n}^e)^{\mathrm{s}}\}, \tag{71}$$

where C is any scalar function. The weighting function for the strain rates thus becomes

$$\nabla^{\mathrm{s}}\boldsymbol{\eta} = \underbrace{\nabla^{\mathrm{s}}\bar{\boldsymbol{\eta}}}_{\text{regular}} + \underbrace{\tilde{\gamma}^h}_{\text{enhanced}}. \tag{72}$$

Because $\widetilde{\mathscr{E}}^h \neq \widetilde{\mathscr{G}}^h$, we have a Petrov–Galerkin formulation.

Substituting (72) into the standard variational equation (12) yields

$$\int_{\Omega^e} \nabla^{\mathrm{s}}\bar{\boldsymbol{\eta}}^h : \dot{\boldsymbol{\sigma}}\,\mathrm{d}\Omega = \int_{\Omega^e} \bar{\boldsymbol{\eta}}^h \cdot \dot{\boldsymbol{f}}\,\mathrm{d}\Omega + \int_{\Gamma^e} \bar{\boldsymbol{\eta}}^h \cdot \dot{\boldsymbol{t}}\,\mathrm{d}\Gamma \tag{73}$$

and

$$\int_{\Omega^e} \tilde{\gamma}^h : \dot{\boldsymbol{\sigma}}\,\mathrm{d}\Omega = 0. \tag{74}$$

For a CST element we see that the patch test

$$\int_{\Omega^e} \tilde{\gamma}^h\,\mathrm{d}\Omega = \boldsymbol{0} \tag{75}$$

is identically satisfied by choosing $C = \mathscr{S}^e/\Omega^e$.

The element matrix equations for the AES method may be written as follows:

$$\begin{bmatrix} \boldsymbol{A}^e_{11} & \boldsymbol{A}^e_{12} \\ \boldsymbol{A}^e_{21} & A^e_{22} \end{bmatrix} \begin{Bmatrix} \dot{\boldsymbol{d}}^e \\ \dot{\zeta}^e \end{Bmatrix} = \begin{Bmatrix} \dot{\boldsymbol{F}}^e_{\mathrm{ext}} \\ 0 \end{Bmatrix}, \tag{76}$$

where

$$\begin{aligned} \boldsymbol{A}^e_{11} &= \int_{\Omega^e} \boldsymbol{B}^{\mathrm{T}}\boldsymbol{D}\boldsymbol{B}\,\mathrm{d}\Omega, \quad \boldsymbol{A}^e_{12} = -\int_{\Omega^e} \boldsymbol{B}^{\mathrm{T}}\boldsymbol{D}\boldsymbol{\beta}\,\mathrm{d}\Omega, \\ \boldsymbol{A}^e_{21} &= -\int_{\Omega^e} \boldsymbol{\alpha}^{\mathrm{T}}\boldsymbol{D}\boldsymbol{B}\mathrm{d}\Omega, \\ A^e_{22} &= \int_{\Omega^e} \boldsymbol{\alpha}^{\mathrm{T}}\boldsymbol{D}\boldsymbol{\beta}\,\mathrm{d}\Omega + \int_{\mathscr{S}^e} \boldsymbol{m}^{eT}\boldsymbol{E}\boldsymbol{m}^e\,\mathrm{d}\mathscr{S} \end{aligned} \tag{77}$$

and $\boldsymbol{\alpha}$ is a vector constructed from the slip tensor $(\boldsymbol{m}^e \otimes \boldsymbol{n}^e)^{\mathrm{s}}$. Comparing to (57) and (58), the Petrov–Galerkin formulation generally yields a nonsymmetric system except when $\nabla f^h(\boldsymbol{x}) \| \boldsymbol{n}^e$ (i.e., the crack is aligned to a side of the triangle), in which case $\boldsymbol{\alpha} = \boldsymbol{\beta}$. As explained in the next section, the relative directions of $\boldsymbol{\alpha}$ and $\boldsymbol{\beta}$ are functions of element orientations relative to the discontinuity surface $\mathscr{S}$. Because slip $\dot{\zeta}^e$ is interpolated by a piecewise constant function, it can be eliminated on the element level by static condensation.

5.2. Galerkin embedded strong discontinuity formulation

A Galerkin embedded strong discontinuity (similar to smeared crack) formulation employing CST elements is demonstrably equivalent to the Petrov–Galerkin AES method [3]. In this formulation, strong discontinuity is introduced into an elastic solid through the use of an anisotropic yield function describing yielding on the crack. The technique does not explicitly use the slip degree of freedom on the element matrix equation; instead, it treats slip on the crack internally. There is no need for static condensation since the elastoplastic stress-strain matrix is already a form of static condensation. Because yielding on the crack is governed by an anisotropic constitutive law, the stress-strain matrix is nonsymmetric, in much the same way that the AES method yields a nonsymmetric system.

We consider the classical variational equation

$$\int_{\Omega^e} \nabla^{\mathrm{s}}\boldsymbol{\eta} : \dot{\boldsymbol{\sigma}}\,\mathrm{d}\Omega = \int_{\Omega^e} \boldsymbol{\eta} \cdot \dot{\boldsymbol{f}}\,\mathrm{d}\Omega + \int_{\Gamma^e} \boldsymbol{\eta} \cdot \dot{\boldsymbol{t}}\,\mathrm{d}\Omega, \tag{78}$$

where $\boldsymbol{\eta}$ is the total weighting function. Slip along a crack introduces an irrecoverable response. This is represented by an anisotropic plasticity model reflecting sliding on the crack.

The Cauchy stress rate in an enhanced elastic solid Ω^e is given by the generalized Hooke's law (see (69))

$$\dot{\boldsymbol{\sigma}} = \boldsymbol{c}^{\mathrm{E}} : [\dot{\bar{\boldsymbol{\epsilon}}} - (\boldsymbol{m}^e \otimes \nabla f^h)^{\mathrm{s}}\dot{\zeta}^e], \quad \dot{\bar{\boldsymbol{\epsilon}}} = \nabla^{\mathrm{s}}\dot{\bar{\boldsymbol{v}}}(\boldsymbol{x}), \quad \boldsymbol{x} \in \Omega^e \setminus \mathscr{S}^e, \tag{79}$$

where $\boldsymbol{c}^{\mathrm{E}}$ is the elastic constitutive tensor (superscript "E" denotes "elastic", in contrast to superscript "e" which pertains to element number). The equation above resembles an additive predictor–corrector split of continuum plasticity in which $\dot{\zeta}^e \geqslant 0$ takes the role of plastic multiplier and $(\boldsymbol{m}^e \otimes \nabla f^h)^{\mathrm{s}}$ is the plastic flow direction.

Let $\mathscr{F}(\boldsymbol{\sigma}, \phi, c) = 0$ denote the yield condition on $\mathscr{S}^e$, where ϕ is the friction angle and c is the cohesion on the crack. For concreteness, we assume the following specific form of the yield condition

$$\mathscr{F}(\boldsymbol{\sigma}, \phi, c) = (\boldsymbol{\mu}^e \otimes \boldsymbol{n}^e)^{\mathrm{s}} : \boldsymbol{\sigma} - c = 0, \tag{80}$$

where

$$\boldsymbol{\mu}^e = \boldsymbol{m}^e + \boldsymbol{n}^e \tan\phi. \tag{81}$$

Note that $\|\boldsymbol{\mu}^e\| = \sqrt{1 + \tan^2\phi} \neq 1$ if $\phi \neq 0$, so $\boldsymbol{\mu}^e$ generally is not a unit vector. Eq. (80) is the Mohr–Coulomb yield criterion on the crack. The consistency condition is

$$\boldsymbol{\psi}^e : \dot{\boldsymbol{\sigma}} - \mathscr{H}_\delta\dot{\zeta}^e = 0, \quad \boldsymbol{\psi}^e = \left.\frac{\partial\mathscr{F}}{\partial\boldsymbol{\sigma}}\right|_{\Omega^e} = (\boldsymbol{\mu}^e \otimes \boldsymbol{n}^e)^{\mathrm{s}}, \tag{82}$$

where $\mathscr{H}_\delta = \partial c/\partial\zeta^e$ is the plastic modulus and $\dot{\zeta}^e$ is the slip rate on $\mathscr{S}^e$. The above equation can be used to solve for the slip rate

$$\dot{\zeta}^e = \frac{(\boldsymbol{\mu}^e \otimes \boldsymbol{n}^e)^{\mathrm{s}} : \boldsymbol{c}^{\mathrm{E}} : \dot{\bar{\boldsymbol{\epsilon}}}}{\boldsymbol{\psi}^e : \boldsymbol{c}^{\mathrm{E}} : (\boldsymbol{m}^e \otimes \nabla f^h)^{\mathrm{s}} + \mathscr{H}_\delta}. \tag{83}$$

We have effectively converted the localization problem into a continuum plasticity problem and the next step is to solve for the stress rate. To this end, we utilize the generalized Hooke's law

$$\dot{\boldsymbol{\sigma}} = \boldsymbol{c}^{\mathrm{EP}} : \nabla^{\mathrm{s}}\dot{\bar{\boldsymbol{v}}}(\boldsymbol{x}), \tag{84}$$

where

$$\boldsymbol{c}^{\mathrm{EP}} = \boldsymbol{c}^{\mathrm{E}} - \frac{\boldsymbol{c}^{\mathrm{E}} : (\boldsymbol{m}^e \otimes \nabla f^h)^{\mathrm{s}} \otimes \boldsymbol{\psi}^e : \boldsymbol{c}^{\mathrm{E}}}{\boldsymbol{\psi}^e : \boldsymbol{c}^{\mathrm{E}} : (\boldsymbol{m}^e \otimes \nabla f^h)^{\mathrm{s}} + \mathscr{H}_\delta}. \tag{85}$$

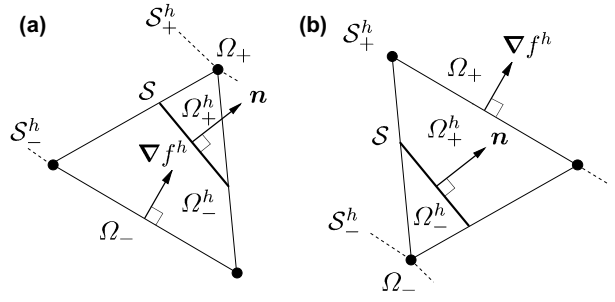

Fig. 6. CST element traced by a discontinuity $\mathscr{S}$: (a) one-node side on the positive side of $\mathscr{S}$; (b) two-node side on the positive side of $\mathscr{S}$. Unit vector $\boldsymbol{n}$ is parallel to ∇f^h when $\mathscr{S}$ is parallel to a side of the triangle.

The matrix form of (78) is readily constructed from the standard Galerkin approximation as

$$\boldsymbol{K}^e\dot{\boldsymbol{d}}^e = \dot{\boldsymbol{F}}^e_{\text{EXT}}, \quad \boldsymbol{K}^e = \int_{\Omega^e} \boldsymbol{B}^{\text{T}}\boldsymbol{D}^{\text{EP}}\boldsymbol{B}\,\mathrm{d}\Omega, \tag{86}$$

where $\boldsymbol{D}^{\text{EP}}$ is the matrix form of $\boldsymbol{c}^{\text{EP}}$. Note that $\boldsymbol{K}^e$ is unsymmetric unless $\boldsymbol{n}^e \| \nabla f^h$ and $\phi = 0$, since the plastic flow direction is different from $\boldsymbol{\psi}^e$.

Equivalence of the present formulation with the AES technique is apparent if we note that for a CST element

$$\boldsymbol{K}^e = \int_{\Omega^e} \boldsymbol{B}^{\text{T}}\boldsymbol{D}^{\text{EP}}\boldsymbol{B}\,\mathrm{d}\Omega = \boldsymbol{A}^e_{11} + \boldsymbol{A}^e_{12}A^{-1}_{22}\boldsymbol{A}^e_{21}, \tag{87}$$

where $\boldsymbol{A}^e_{11}$, $\boldsymbol{A}^e_{12}$, $\boldsymbol{A}^e_{21}$, and A^e_{22} are element matrices defined in (77), with the constitutive matrix $\boldsymbol{D}$ replaced by the elastic component $\boldsymbol{D}^{\text{E}}$. Clearly, the constitutive law on the slip surface determines the appropriate weighting function for the AES method. If $\phi = 0$, then we recover the weighting function used in [30].

Fig. 6 shows the physical meanings of the vectors ∇f^h and $\boldsymbol{n}^e$ for an enhanced CST element. A well traced CST element has a side parallel to the slip line, in which case, $\nabla f^h \| \boldsymbol{n}^e$. In contrast, a poorly traced CST element has a side that may be significantly skewed from the slip line. The latter condition could cause some ill-conditioning problems, see [3].

6. Numerical examples

In this section we present numerical examples involving tangential sliding of an elastic solid along a cohesive–frictional crack. The examples focus only on the AES and extended FE solutions, but in one of the examples we shall also report some results obtained using classical contact mechanics FE analysis to highlight the similarity with the extended FE solutions. For the most part we shall only consider a Heaviside enhancement since the AES algorithm cannot handle crack tip enrichment due to the assumed piecewise constant interpolation of slip. Toward the end of the section we shall demonstrate the important role played by crack tip enrichment toward an accurate prediction of slip with the extended FE method. As for the AES method, we utilize the Galerkin embedded strong discontinuity formulation of Section 5.2 in the simulations. Deformations are assumed to be infinitesimal in all the examples.

Some remarks on the crack slip simulation are in order. In the AES method the plastic flow direction, represented by the slip tensor $(\boldsymbol{m}^e \otimes \boldsymbol{n}^e)^{\text{s}}$, is explicitly specified for each enhanced element. In the extended FE solution, on the other hand, the plastic flow direction is enforced by penalization at the Gauss points lying on the crack. The algorithm utilized for frictional crack problem with the extended FE solution is described by Liu and Borja [20]. The algorithm essentially mimics the stick-slip feature of nonlinear contact mechanics [68–70] except that slave-master sides are now used instead of the usual slave node-master segment format since the contact constraints are now embedded in the interior of the CST elements. For infinitesimal plane strain deformation, the slip tensor is fixed for each localizing element. Hence, once the active constraints have been properly identified all solutions theoretically require only one Newton–Raphson iteration to converge.

In the numerical examples below we assume the following material parameters (consistent units are implied throughout): Young's modulus $E = 10^5$ and Poisson's ratio $\nu = 0.30$ for the elastic solid; normal and tangential penalty parameters for the extended FE solution are $\epsilon_N = \epsilon_T = 10^7$. Yielding on the crack follows the Mohr–Coulomb yield criterion with cohesion c and friction angle ϕ (coefficient of friction $= \tan\phi$).

6.1. Uniform slip

The boundary-value problem consists of a 2×4 (width/height) elastic solid with a 45° crack passing through the point $(0.0, 0.7)$, assuming the bottom left corner of the solid passes through the origin. In Fig. 7 we show three FE element meshes: mesh 1 has 15 nodes and 16 CST elements; mesh 2 has 153 nodes and 256 elements; and mesh 3 has 561 nodes and 1024 elements. The figure also shows the crack terminating at coordinate $(1.3, 2.0)$ and the enhanced CST elements are represented by the shaded region. As a

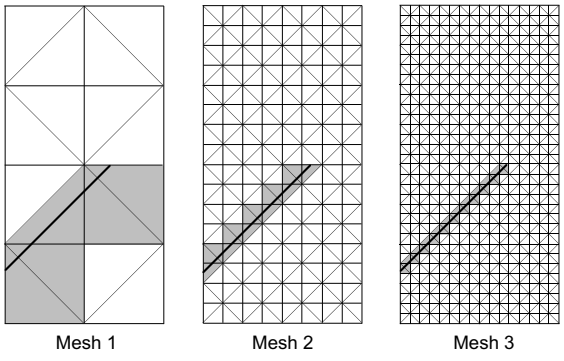

Fig. 7. Plane strain rectangular body with a fixed crack: finite element meshes. Crack is represented by the solid thick line. The support of $M_{\mathscr{S}}(\boldsymbol{x})$ is denoted by the shaded triangles.

preliminary step, however, we first assume that the crack cuts through the entire solid up to the point (2.0, 2,7) on the right vertical side and compress the solid vertically by prescribing a uniform displacement of 0.10 on top, assuming that the top and bottom surfaces of the solid are smooth and the two vertical sides are traction-free. The friction angle on the crack is assumed to be $\phi = 5.71°$ (coefficient of friction = 0.10).

Under the imposed deformation described above, Fig. 8 shows identical uniform slip calculated by the AES and extended FE solutions. The magnitude of slip varies with cohesion c, and Fig. 8 shows the calculated uniform slip when $c = 500$. The magnitude of uniform slip ζ decreases linearly with cohesion c as can be seen from Fig. 9. When $c = 0$, the stress throughout the body during slip activation is zero, and so $\zeta = 0.10\sqrt{2} = 0.1414$. This is the maximum possible slip at any point on the 45°-crack when the vertical compression is 0.10.

6.2. Nonuniform slip and crack tip deformation

We now consider the case of a finite stationary crack shown in Fig. 7. Once again, we compress the solid to a vertical compression of 0.10. Figs. 10–12 show variations of slip generated by the AES and extended FE solutions

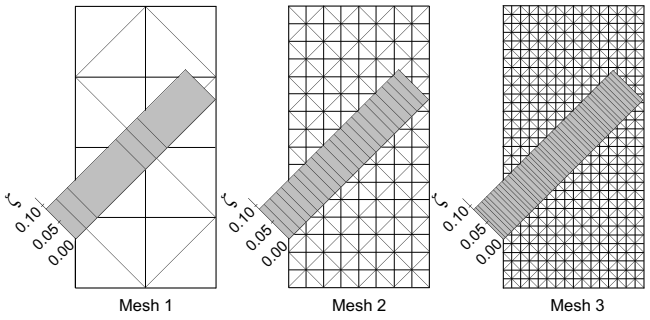

Fig. 8. Uniform slip produced by a crack that cuts through the entire body. Constitutive parameters for the crack are: cohesion $c = 500$ stress units and friction angle $\phi = 5.71°$ (coefficient of friction = 0.10). AES and extended FE methods produced identical results.

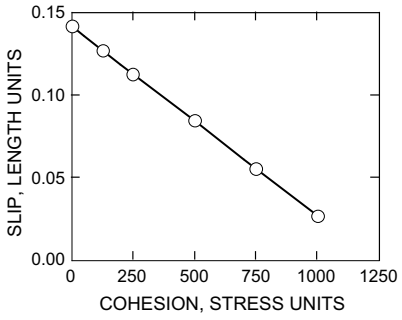

Fig. 9. Variation of slip (uniform throughout the crack) for a crack with cohesion c and friction angle $\phi = 5.71°$ (coefficient of friction = 0.10).

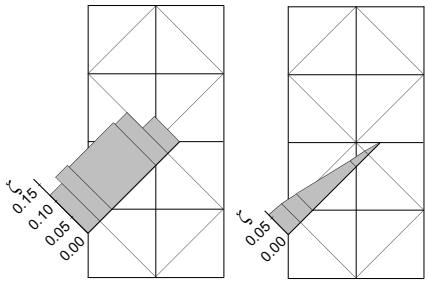

Fig. 10. Variation of slip on a finite crack generated by the AES method (left) and extended FE solution (right) with Mesh 1. Constitutive parameters for the crack are: cohesion $c = 0$ and friction angle $\phi = 5.71°$.

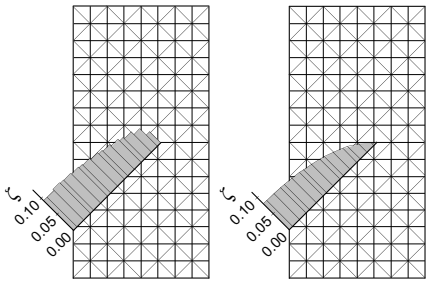

Fig. 11. Variation of slip on a finite crack generated by the AES method (left) and extended FE solution (right) with Mesh 2. Constitutive parameters for the crack are: cohesion $c = 0$ and friction angle $\phi = 5.71°$.

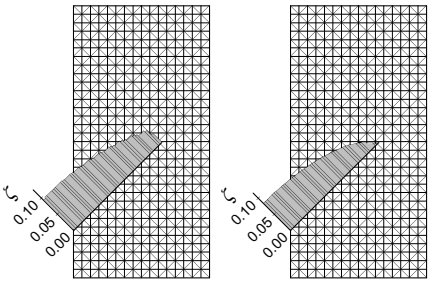

Fig. 12. Variation of slip on a finite crack generated by the AES method (left) and extended FE solution (right) with Mesh 3. Constitutive parameters for the crack are: cohesion $c = 0$ and friction angle $\phi = 5.71°$.

using meshes 1–3, respectively. In general, the AES solutions predict softer responses (i.e., larger slip) with coarser meshes, whereas the extended FE solution predicts stiffer responses (i.e., smaller slip). However, as the mesh is refined further the two methods appear to converge to two different solutions, with the AES solution predicting a nearly elliptical slip distribution consistent with linear elastic fracture mechanics theory [9,49,56], and the extended FE solution predicting a bullet-shaped slip distribution, see Figs. 11 and 12. Because the extended FE solution is unable to capture the steep gradient near the crack tip with only a Heaviside enrichment, the calculated slip is smaller than that obtained with the AES solution everywhere on the crack.

To further elaborate the discrepancy between the two sets of solution shown in Figs. 10–13, we show in Fig. 14 deformation details around the crack tip calculated by the extended FE method. As the rectangular solid is vertically compressed, the crack tries to slip but is prevented from doing so by the fixed crack tip. Therefore, to accommodate the imposed deformation the crack has to open up near the tip even if the imposed overall deformation is a vertical compression. In a way, this crack tip element tends to "lock". The kinematics of deformation is confirmed in Fig. 14 which compares the deformed meshes generated by the AES and extended FE solutions: the two deformed meshes are nearly the same except near the crack tip where the calculated vertical downward movement is less with the extended FE solution (due to the "locking" mode). Since the AES solution was formulated precisely to avoid locking, the solution does not exhibit an opening mode.

6.3. Comparison with nonlinear contact mechanics solution

One might guess that the solution provided by the extended FE method is essentially the same as that generated by classical contact mechanics algorithm when the crack traverses the element sides since the two methods utilize essentially the same displacement interpolations. We thus consider a 45° finite crack that passes very close to the element sides as shown in Fig. 15. In classical contact mechanics the crack is represented by slave node/master segment contact elements [68–70], so in this case the crack may be prescribed to pass exactly through the nodes. To this end, we consider a straight crack with tips at coordinates $(0.00, 1.00)$ and $(1.75, 2.75)$ in Fig. 15 (again, the lower left-hand corner of the rectangle is placed at the origin). On the other hand, with the AES and extended FE methods the crack may not pass exactly through the nodes, so we consider instead an adjacent crack with tips at points $(0.0, 0.99)$ and $(1.75, 2.74)$ and passing through the interior of the finite elements.

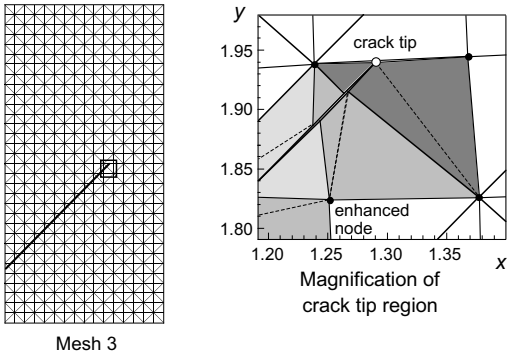

Fig. 13. Detail of crack tip region generated by the extended FE solution. To accommodate slip, the crack opens up near the crack tip even if the mesh is compressed in the vertical direction. Shaded triangles form part of the support of $M_{\mathscr{S}}(\boldsymbol{x})$. Dashed lines define subtriangles used for numerical integration. Dark circles denote enhanced nodes; open circle is crack tip.

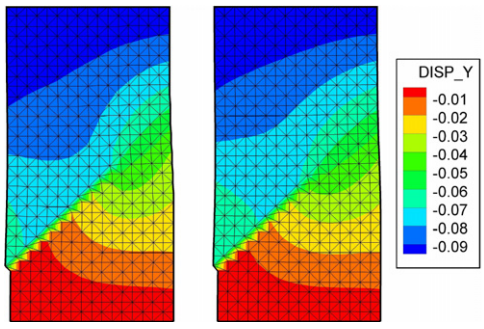

Fig. 14. Deformed meshes and vertical displacement contours generated by the AES method (left) and the extended FE solution (right).

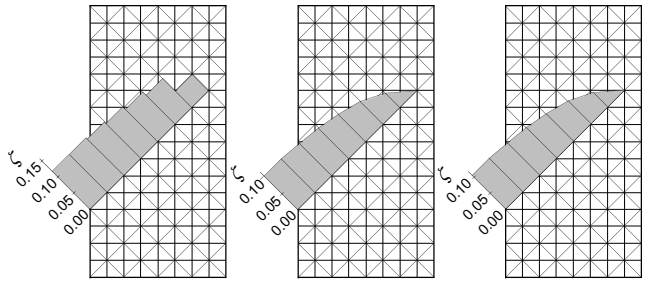

Fig. 15. Variation of slip on a finite crack adjacent to element sides generated by the AES (left), extended FE (middle), and classical contact mechanics (right) solutions. Constitutive parameters for the crack are: cohesion $c = 0$ and friction angle $\phi = 5.71°$.

Fig. 16 shows that the variation of slip predicted by the extended FE and classical contact mechanics solutions are essentially the same, with the AES solution again predicting larger slip (softer response) particularly near the crack tip. The small discrepancy between the extended FE and contact mechanics solutions may be attributed to minor differences in the implementation: the extended FE solution imposes contact condition at the Gauss points on the crack, whereas the nonlinear contact mechanics solution imposes the constraint at the node-to-segment contact. As in the previous example, the slip distribution predicted by the AES method shows the classical elliptical shape

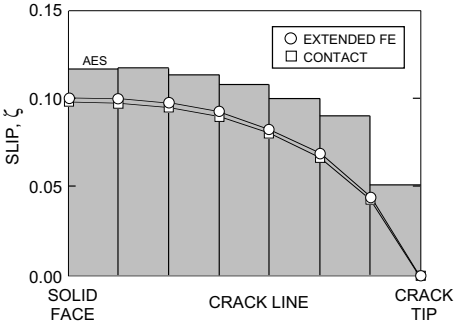

Fig. 16. Variation of slip for a finite crack adjacent to element sides. The crack has zero cohesion and friction angle $\phi = 5.71°$. Nonlinear contact mechanics and extended FE solutions enriched with a Heaviside function predict nearly the same slip distributions that are about 20% smaller than that predicted by the AES method.

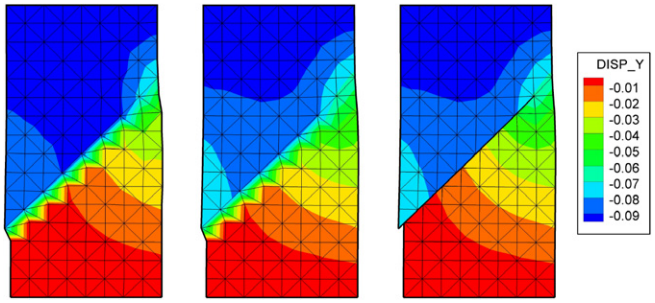

Fig. 17. Deformed FE meshes for the problem of a finite crack adjacent to element sides: AES (left), extended FE (middle), and classical contact mechanics (right). Note that the conforming deformation exhibited by the classical contact mechanics solution shows a sharp discontinuity along the crack.

consistent with linear elastic fracture mechanics theory, whereas the extended FE and classical contact mechanics solutions show bullet-shaped slip distributions. The deformed meshes predicted by the three methods are shown in Fig. 17, with the extended FE and nonlinear contact mechanics solutions again manifesting a tendency to dilate (or lock) in the vicinity of the crack tip to allow the slip to build up rapidly in that area. Note that the deformed meshes only show conforming deformations; if displacement discontinuities were explicitly plotted the deformed meshes for the extended FE and nonlinear contact mechanics solutions would be practically the same.

6.4. Crack tip enrichment

In this section we investigate the role played by the crack tip enrichment on the numerical values of slip calculated by the extended FE method. We recall from linear elastic fracture mechanics [56,2] that the near-tip displacement field for combined Modes I and II loading are

$$u(r,\theta) = \frac{K_{\mathrm{I}}}{2\mu}\sqrt{r/2\mu}\cos\left(\frac{\theta}{2}\right)\left[\kappa - 1 + 2\sin^2\left(\frac{\theta}{2}\right)\right] + \frac{K_{\mathrm{II}}}{2\mu}\sqrt{r/2\mu}\sin\left(\frac{\theta}{2}\right)\left[\kappa + 1 + 2\cos^2\left(\frac{\theta}{2}\right)\right] \tag{88}$$

for the x direction, and

$$v(r,\theta) = \frac{K_{\mathrm{I}}}{2\mu}\sqrt{r/2\mu}\sin\left(\frac{\theta}{2}\right)\left[\kappa + 1 - 2\cos^2\left(\frac{\theta}{2}\right)\right] - \frac{K_{\mathrm{II}}}{2\mu}\sqrt{r/2\mu}\cos\left(\frac{\theta}{2}\right)\left[\kappa - 1 - 2\sin^2\left(\frac{\theta}{2}\right)\right] \tag{89}$$

for the y direction, where

$$\kappa = \begin{cases} 3 - 4\nu, & \text{plane strain} \\ (3-\nu)/(1+\nu), & \text{plane stress} \end{cases} \tag{90}$$

is the Kolosov constant. In the above equations, K_{I} and K_{II} are stress intensity factors, r and θ are cylindrical coordinates originating from the crack tip, ν is the Poisson's ratio, and μ is the elastic shear modulus. The angle θ ranges from $-\pi$ to $+\pi$ ($\theta = 0$ is the crack line pointing away from the tip) so that $\sin(\theta/2)$ represents the discontinuous function on the crack. For pure Mode II loading the near-tip slip is given by

$$\zeta(r) = u(r,\pi) - u(r,-\pi) = \frac{K_{\mathrm{II}}}{\mu}(\kappa+1)\sqrt{r/2\mu}. \tag{91}$$

The gradient of slip with respect to r is

$$\zeta'(r) = \frac{K_{\mathrm{II}}}{2\mu}\frac{\kappa+1}{\sqrt{2\mu r}}. \tag{92}$$

The above equation shows a $1/\sqrt{r}$ near-tip singularity of the gradient of slip. This singularity cannot be captured by conventional finite elements used in the extended FE solution, and thus Figs. 10–12, for example, show that no matter how one refines the mesh the gradient of slip at the crack tip remains finite. The same can be said of the classical contact mechanics FE solution. In contrast, values of slip predicted by the AES solution (see same figures) show infinite gradients at the crack tip.

Special finite elements have been proposed in the past to handle crack tip singularity in linear elastic fracture mechanics (see [72]). Here we enrich the description of near-tip displacement field through a technique proposed in [2]. The technique requires the introduction of additional nodal degrees of freedom for the polygonal support of the crack tip to accommodate four near-tip shape functions described by the span

$$\gamma_i(r,\theta) = \sqrt{r} f_i, \quad f_1 = \cos\left(\frac{\theta}{2}\right), \quad f_2 = \sin\left(\frac{\theta}{2}\right), \quad f_3 = \sin\left(\frac{\theta}{2}\right)\sin\theta, \quad f_4 = \cos\left(\frac{\theta}{2}\right)\sin\theta. \tag{93}$$

Fig. 18 shows the 'improved' slip distribution calculated by the extended FE element solution utilizing both the Heaviside and crack tip enrichment functions for the boundary-value problem depicted in Fig. 15. It is evident that the crack tip enrichment alleviates near-tip locking of conventional finite elements and now accommodates a vertical slope at the crack tip. It is noteworthy that the AES and ex-

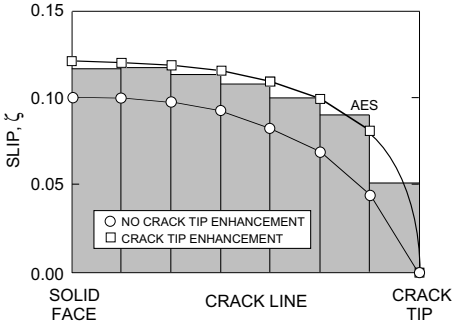

Fig. 18. Variation of slip for a finite crack adjacent to element sides. The crack has zero cohesion and friction angle $\phi = 5.71°$. Extended FE solution enriched with only the Heaviside function predicts a slip distribution that is about 20% smaller than that predicted by the AES method. With a crack tip enrichment, the extended FE solution predicts nearly the same slip distribution as the AES method.

tended FE solutions (with Heaviside and crack tip enhancements) predict nearly the same slip distributions despite the fact that the former technique employs a much simpler kinematical enrichment. For the record, the final numerical values of solid-face slip are as follows: 0.101 (Heaviside only) and 0.120 (Heaviside plus crack tip enrichments) for the extended FE method, and 0.118 for the AES method.

7. Summary and conclusions

We have presented strong and weak forms of boundary-value problem for a solid with a discontinuity represented by a jump in the velocity field. The variational equation was used to construct finite element approximations to two kinematical variables: the regular velocity field $\bar{\boldsymbol{v}}$ defined throughout the domain Ω, and the discontinuous velocity field $\tilde{\boldsymbol{v}}$ defined inside the support of $M_{\mathscr{S}}$. The AES method is recovered from a Petrov–Galerkin formulation, resulting in a piecewise constant interpolation of slip. The Galerkin embedded strong discontinuity method reformulates the AES approach in a way that resembles a classical continuum plasticity solution in the post-localization regime requiring modification to the material subroutine only. The extended FE method is recovered from a Galerkin formulation expressed in terms of relative displacement on the crack, giving rise to slip interpolation that is continuous across element boundaries. Along with classical nonlinear contact mechanics theory, the aforementioned enhanced FE methods have been implemented into a common platform so that the numerical solutions may be compared for the case of two-dimensional plane strain boundary-value problems utilizing the basic constant strain triangular elements.

Based on the numerical examples presented, with only a Heaviside enrichment the AES solution predicts larger slip (i.e., softer response) than the extended FE solution, and is able to capture the elliptical shape slip distribution predicted by classical linear elastic fracture mechanics theory. This may be attributed to the piecewise constant slip interpolation that allows the steep displacement gradient to be smeared throughout the finite element volume surrounding the crack tip area, thus circumventing the tendency of the crack tip elements to lock. On the other hand, the extended FE and classical nonlinear contact mechanics solutions predict bullet-shaped slip distributions, suggesting that with these methods the Heaviside enhancement alone would not be sufficient to capture the steep gradients near the crack tip. Indeed, it has been demonstrated that by introducing the crack tip enrichment functions the slip distribution calculated by the extended FE method has improved to be comparable to that obtained with the AES method. We note from the limited examples considered in this paper that slip calculated near the crack tip impacts those calculated throughout the crack, so it is important to capture the steep displacement gradient near the crack tip. Finally, we note that this paper is far from being complete in that we have yet to consider other important aspects such as crack tip plasticity (both small- and large-scale yielding), finite deformation, and three-dimensional loading, among others. Research on some of these aspects is currently in progress.

Acknowledgements

This work is supported by the US Department of Energy Grant No. DE-FG02-03ER15454, and National Science Foundation Grant No. CMG-0417521 (Collaborations in Mathematical Geosciences). The author is grateful to graduate students Fushen Liu and Pablo Sanz for assistance in running some of the numerical problems. He is also very grateful to three anonymous reviewers for their expert reviews.

References

[1] F. Armero, K. Garikipati, Recent advances in the analysis and numerical simulation of strain localization in inelastic solids, in: D.R.J. Owen, E. Oñate, E. Hinton (Eds.), Proceedings of Computational Plasticity IV, CIMNE, Barcelona, Spain, 1995, pp. 547–561.
[2] T. Belytschko, T. Black, Elastic crack growth in finite elements with minimal remeshing, Int. J. Numer. Meth. Engrg. 45 (1999) 601–620.
[3] R.I. Borja, A finite element model for strain localization analysis of strongly discontinuous fields based on standard Galerkin approximations, Comput. Meth. Appl. Mech. Engrg. 190 (2000) 1529–1549.
[4] R.I. Borja, R.A. Regueiro, Strain localization in frictional materials exhibiting displacement jumps, Comput. Meth. Appl. Mech. Engrg. 190 (2001) 2555–2580.
[5] R.I. Borja, Finite element simulation of strain localization with large deformation: capturing strong discontinuity using a Petrov–Galerkin multiscale formulation, Comput. Meth. Appl. Mech. Engrg. 191 (2002) 2949–2978.
[6] Z. Chessa, H. Wang, T. Belytschko, On the construction of blending elements for local partition of unity enriched finite elements, Int. J. Numer. Meth. Engrg. 57 (2003) 1015–1038.
[7] F. Darve, G. Servant, F. Laouafa, H.D.V. Khoa, Failure in geomaterials: continuous and discrete analyses, Comput. Meth. Appl. Mech. Engrg. 193 (2004) 3057–3085.
[8] J. Dolbow, N. Möes, T. Belytschko, An extended finite element method for modeling crack growth with frictional contact, Comput. Meth. Appl. Mech. Engrg. 190 (2001) 6825–6846.
[9] A. Dorogoy, L. Banks-Sills, Shear loaded interface crack under the influence of friction: a finite difference solution, Int. J. Numer. Meth. Engrg. 59 (2004) 1749–1780.
[10] E.N. Dvorkin, A.M. Cuitino, G. Gioia, Finite elements with displacement interpolated embedded localization lines insensitive to mesh size and distortions, Int. J. Numer. Meth. Engrg. 30 (1990) 541–564.
[11] E.N. Dvorkin, A.P. Assanelli, 2D finite elements with displacement interpolated embedded localization lines: the analysis of fracture in frictional materials, Comput. Meth. Appl. Mech. Engrg. 90 (1991) 829–844.
[12] P.H. Feenstra, R. de Borst, A plasticity model and algorithm for mode-I cracking in concrete, Int. J. Numer. Meth. Engrg. 38 (1995) 2509–2529.
[13] C. Feist, G. Hofstetter, An embedded strong discontinuity model for cracking of plain concrete, Comput. Meth. Appl. Mech. Engrg. 195 (2006) 7115–7138.
[14] C.D. Foster, R.I. Borja, R.A. Regueiro, Embedded strong discontinuity finite elements for fractured geomaterials with variable friction, Int. J. Numer. Meth. Engrg. 72 (2007) 549–581.

[15] M. Jirásek, Comparative study on finite elements with embedded discontinuities, Comput. Meth. Appl. Mech. Engrg. 188 (2000) 307–330.
[16] A.R. Khoei, A. Shamloo, A.R. Azami, Extended finite element method in plasticity forming of powder compaction with contact friction, Int. J. Solids Struct. 43 (2006) 5421–5448.
[17] T.Y. Kim, J. Dolbow, T. Laursen, A mortared finite element method for frictional contact on arbitrary interfaces, Comput. Mech. 39 (2007) 223–235.
[18] P.A. Klerck, E.J. Sellers, D.R.J. Owen, Discrete fracture in quasi-brittle materials under compressive and tensile stress states, Comput. Meth. Appl. Mech. Engrg. 193 (2004) 3035–3056.
[19] R. Larsson, K. Runesson, S. Sture, Embedded localization band in undrained soil based on regularized strong discontinuity theory and FE analysis, Int. J. Solids Struct. 33 (1996) 3081–3101.
[20] F. Liu, R.I. Borja, A contact algorithm for frictional crack propagation with the extended finite element method, Int. J. Numer. Meth. Engrg. in press, doi: 10.1002/nme.2376.
[21] G. Meschke, P. Dumstorff, Energy-based modeling of cohesive and cohesionless cracks via X-FEM, Comput. Meth. Appl. Mech. Engrg. 196 (2007) 2338–2357.
[22] N. Moës, T. Belytschko, Extended finite element method for cohesive crack growth, Engrg. Frac. Mech. 69 (2002) 813–833.
[23] J. Oliver, A.E. Huespe, Continuum approach to material failure in strong discontinuity settings, Comput. Meth. Appl. Mech. Engrg. 193 (2004) 3195–3220.
[24] J. Oliver, A.E. Huespe, P.J. Sánchez, A comparative study on finite elements for capturing strong discontinuities: E-FEM vs. X-FEM, Comput. Meth. Appl. Mech. Engrg. 195 (2006) 4732–4752.
[25] M. Ortiz, Y. Leroy, A. Needleman, A finite element method for localized failure analysis, Comput. Meth. Appl. Mech. Engrg. 61 (1987) 189–214.
[26] R.A. Regueiro, R.I. Borja, Plane strain finite element analysis of pressure-sensitive plasticity with strong discontinuity, Int. J. Solids Struct. 38 (2001) 3647–3672.
[27] M.R. Salari, S. Saeb, K.J. Willam, S.J. Patchet, R.C. Carrasco, A coupled elastoplastic damage model for geomaterials, Comput. Meth. Appl. Mech. Engrg. 193 (2004) 2625–2643.
[28] J.C. Simo, M.S. Rifai, A class of mixed assumed strain methods and the method of incompatible modes, Int. J. Numer. Meth. Engrg. 29 (1990) 1595–1638.
[29] J.C. Simo, J. Oliver, F. Armero, An analysis of strong discontinuities induced by strain-softening in rate-independent inelastic solids, Comput. Mech. 12 (1993) 277–296.
[30] J.C. Simo, J. Oliver, A new approach to the analysis and simulation of strain softening in solids, in: Z.P. Bažant, Z. Bittnar, M. Jirásek, J. Mazars (Eds.), Fracture and Damage in Quasibrittle Structures, E&FN Spon, London, 1994.
[31] A. Simone, L.J. Sluys, The use of displacement discontinuities in a rate-dependent medium, Comput. Meth. Appl. Mech. Engrg. 193 (2004) 3015–3033.
[32] N. Sukumar, J.H. Prevost, Modeling quasi-static crack growth with the extended finite element method part I: computer implementation, Int. J. Solids Struct. 40 (2003) 7513–7537.
[33] J.F. Unger, S. Eckardt, C. Könke, Modelling of cohesive crack growth in concrete structures with the extended finite element method, Comput. Meth. Appl. Mech. Engrg. 196 (2007) 4087–4100.
[34] G.N. Wells, L.J. Sluys, Three-dimensional embedded discontinuity model for brittle fracture, Int. J. Solids Struct. 38 (2001) 897–913.
[35] G.N. Wells, R. de Borst, L.J. Sluys, A consistent geometrically non-linear approach for delamination, Int. J. Numer. Meth. Engrg. 54 (2002) 1333–1355.
[36] A. Aydin, R.I. Borja, P. Eichhubl, Geological and mathematical framework for failure modes in granular rock, J. Struct. Geol. 28 (2006) 83–98.
[37] T. Baxevanis, E. Papamichos, O. Flornes, I. Larsen, Compaction bands and induced permeability reduction in Tuffeau de Maastricht calcarenite, sech. 1 (2006) 123–135.
[38] P. Bésuelle, Compacting and dilating shear bands in porous rock: theoretical and experimental conditions, J. Geophys. Res. 106 (2001) 13435–13442.
[39] R.I. Borja, A. Aydin, Computational modeling of deformation bands in granular media. I. Geological and mathematical framework, Comput. Meth. Appl. Mech. Engrg. 193 (2004) 2667–2698.
[40] R.I. Borja, Computational modeling of deformation bands in granular media. II. Numerical simulations, Comput. Meth. Appl. Mech. Engrg. 193 (2004) 2699–2718.
[41] R.I. Borja, Conditions for instabilities in collapsible solids including volume implosion and compaction banding, Acta Geotech. 1 (2006) 107–122.
[42] D. Holcomb, J.W. Rudnicki, K.A. Issen, K. Sternlof, Compaction localization in the Earth and the laboratory: state of the research and research directions, Acta Geotech. 2 (2007) 1–15.
[43] K.A. Issen, J.W. Rudnicki, Conditions for compaction bands in porous rock, J. Geophys. Res. 105 (2000) 21529–21536.
[44] M.S. Paterson, T. Wong, Experimental Rock Deformation – The Brittle Field, second ed., Springer, 2005.
[45] J.W. Rudnicki, Conditions for compaction and shear bands in a transversely isotropic material, Int. J. Solids Struct. 39 (2002) 3741–3756.
[46] K.R. Sternlof, Structural geology, propagation mechanics and hydraulic effects of compaction bands in sandstone, PhD Thesis, Stanford University, 2006.
[47] V. Vajdova, T. Wong, Incremental propagation of discrete compaction bands: acoustic emission and microstructural observations on circumferentially notched samples of Bentheim sandstone, Geophys. Res. Lett. 30 (2003) 1775, doi:10.1029/2003GL017750.
[48] J.D. Byerlee, Theory of friction based on brittle fracture, J. Appl. Phys. 38 (1967) 2928–2934.
[49] M.L. Cooke, Fracture localization along faults with spatially varying friction, J. Geophys. Res. 102 (1996) 22425–22434.
[50] C. Marone, C.B. Raleigh, C.H. Scholz, Frictional behavior and constitutive modeling of simulated fault gouge, J. Geophys. Res. 95 (1990) 7007–7025.
[51] O. Mutlu, A. Bobet, Slip propagation along frictional discontinuities, Int. J. Rock Mech. Min. Sci. 43 (2006) 860–876.
[52] C.A. Queener, T.C. Smith, W.L. Mitchell, Transient weak of machine parts, Wear 8 (1965) 391–400.
[53] C.H. Scholz, The Mechanics of Earthquakes and Faulting, Cambridge University Press, New York, 1990.
[54] K. Xia, A.J. Rosakis, H. Kanamori, J.R. Rice, Laboratory earthquakes along inhomogeneous faults: directionality and supershear, Science 308 (2005) 681–684.
[55] Z.P. Bažant, J. Planas, Fracture and Size Effect in Concrete and Other Quasibrittle Materials, CRC Press, New York, 1998.
[56] D. Broek, Elementary Engineering Fracture Mechanics, Martinus Nijhoff Publishers, Boston, 1982.
[57] J.H. Dieterich, Modeling of rock friction 1. Experimental results and constitutive equations, J. Geophys. Res. 84 (1979) 2161–2168.
[58] J.H. Dieterich, B.D. Kilgore, Imaging surface contacts: power law contact distributions and contact stresses in quartz, calcite, glass and acrylic plastic, Tectonophysics 256 (1996) 219–239.
[59] A.L. Ruina, Slip instability and state variable friction laws, J. Geophys. Res. 88 (1983) 10359–10370.
[60] C.H. Scholz, Earthquake and friction laws, Nature 391 (1998) 37–42.
[61] R. de Borst, Some recent issues in computational failure mechanics, Int. J. Numer. Meth. Engrg. 52 (2001) 63–95.
[62] J. Mosler, G. Meschke, 3D modelling of strong discontinuities in elastoplastic solids: fixed and rotating localization formulations, Int. J. Numer. Meth. Engrg. 57 (2003) 1553–1576.
[63] M. Jirásek, T. Zimmermann, Embedded crack model: I. Basic formulation, Int. J. Numer. Meth. Engrg. 50 (2001) 1269–1290.
[64] M. Jirásek, T. Zimmermann, Embedded crack model. Part II: combination with smeared cracks, Int. J. Numer. Meth. Engrg. 50 (2001) 1291–1305.

[65] J.M. Melenk, I. Babuška, The partition of unity finite element method: basic theory and applications, Comput. Meth. Appl. Mech. Engrg. 39 (1996) 289–314.
[66] I. Babuška, J.M. Melenk, The partition of unity method, Int. J. Numer. Meth. Engrg. 40 (1997) 727–758.
[67] P. Ladevèze, Nonlinear Computational Structural Mechanics, Springer, New York, 1998.
[68] T.A. Laursen, J.C. Simo, A continuum-based finite element formulation for the implicit solution of multibody, large deformation frictional contact problems, Int. J. Numer. Meth. Engrg. 36 (1993) 3451–3485.
[69] P.F. Sanz, R.I. Borja, D.D. Pollard, Mechanical aspects of thrust faulting driven by far-field compression and their implications for fault geometry, Acta Geotech. 2 (2007) 17–31.
[70] P. Wriggers, Computational Contact Mechanics, Wiley, Chischester, 2002.
[71] T.J.R. Hughes, The Finite Element Method, Prentice-Hall, Englewood Cliffs, NJ, 1987.
[72] J.R. Rice, D.M. Tracey, Computational fracture mechanics, in: S.J. Fenves et al. (Eds.), Numerical and Computer Methods in Structural Mechanics, Academic Press, New York, 1973, pp. 585–623.